EES Catalysis

ROYAL SOCIETY OF CHEMISTRY

REVIEW ARTICLE

View Article Online
View Journal | View Issue

Cite this: *EES Catal.*, 2025, **3**, 235

Ammonia synthesis from nitrate reduction by the modulation of a built-in electric field and external stimuli

Shaoce Zhang,[a] Rong Zhang,[a] Ying Guo[b] and Chunyi Zhi *[acde]

Ammonia (NH_3) is a vital chemical feedstock and a carbon-free energy source. The reduction of nitrate (NO_3^-) from environmental pollutants is a sustainable method for NH_3 production compared with the industrially intensive Haber–Bosch method, which can mitigate energy and environmental concerns. However, due to the involvement of multi-electron transfer-proton coupling processes, the NO_3^- reduction reaction (NO_3RR) exhibits sluggish kinetics and significant side reactions. This review provides a comprehensive summary of recent research progress in facilitating NO_3RRs using a built-in electric field and external stimuli. The paper commences by introducing the mechanisms and challenges of the NO_3RR, subsequently focusing on strategies for built-in electric field/external stimuli-assisted catalytic reactions. The internal electric field can be triggered by constructing a Mott–Schottky heterojunction and a semiconductor–semiconductor heterojunction, adjusting the coordination environment of active sites, and regulating the electrical double layer, while the external stimuli include optical, stress, and thermal stimuli. This review focuses on the activation and adsorption processes of reactants and intermediates by a built-in electric field/external stimuli, and their influence on the thermodynamics and kinetics of reactions. Finally, we summarize the strategies for built-in electric field/external stimuli-assisted NO_3RRs, highlight the challenges of achieving high activity and selectivity in NH_3 production, and provide clear guidance for future research.

Received 9th November 2024,
Accepted 3rd January 2025

DOI: 10.1039/d4ey00245h

rsc.li/eescatalysis

Broader context

Ammonia (NH_3) plays an essential role in agriculture, industry, and pharmaceuticals, with its global demand greatly increasing. However, traditional NH_3 production relies on the energy-intensive Haber–Bosch process, which involves nitrogen and hydrogen as raw materials under high-temperature, high-pressure conditions, resulting in significant CO_2 emissions. The aqueous-based reduction of NO_3^- utilizes water and the pollutant NO_3^- as raw materials, converting them into NH_3 through various forms of energy input such as electrocatalysis and photocatalysis. This process concurrently addresses both energy crises and environmental pollution issues. However, the NO_3^- reduction reaction (NO_3RR) to generate NH_3 involves a nine-proton and eight-electron transfer process, leading to sluggish kinetics and severely competitive hydrogen evolution. Therefore, multiple strategies have been proposed to enhance the performance of NO_3^- reduction. Among them, introducing a built-in electric field/external stimuli to modulate the activation and adsorption behavior of reactants and intermediates, thereby promoting reaction kinetics and thermodynamics, becomes a promising strategy. Based on this, this review provides a comprehensive summary of the latest research progress in built-in electric field/external stimuli-assisted NO_3RRs, including material analysis, mechanistic elucidation, problem summarization, and future prospects. This review aims to facilitate NO_3RR performance and provide guidance for NO_3RR processes in future industrial implementations.

1. Introduction

Ammonia (NH_3) is indispensable in fertilizer manufacturing and the pharmaceutical industry, and it is a promising energy carrier because of its high hydrogen content.[1–4] However, the production of NH_3 currently relies heavily on the industrially intensive Haber–Bosch process, which requires high pressure and high temperatures, leading to significant greenhouse gas emissions.[5–7] Therefore, aqueous-based NH_3 synthesis, utilizing water molecules as proton sources and nitrogen gas (N_2)/

---

[a] Department of Materials Science and Engineering, City University of Hong Kong, 83 Tat Chee Avenue, Kowloon, Hong Kong 999077, China. E-mail: cy.zhi@cityu.edu.hk
[b] School of Interdisciplinary Studies, Lau Chun Him Building, Lingnan University, 8 Castle Peak Road, Tuen Mun, New Territories, Hong Kong, China
[c] Hong Kong Center for Cerebro-Cardiovascular Health Engineering (COCHE), Shatin, NT, HKSAR, China
[d] Centre for Functional Photonics, City University of Hong Kong, Kowloon, Hong Kong, China
[e] Hong Kong Institute for Clean Energy, City University of Hong Kong, Kowloon 999077, Hong Kong, China

nitrate ions (NO_3^-) as nitrogen sources, has garnered widespread attention.[8–10] In comparison to the high dissociation energy of the N≡N bond in nitrogen molecules (941 kJ mol^{-1}), the dissociation energy of the N=O bond is only 204 kJ mol^{-1},[11] which suggests that the NO_3^- reduction reaction (NO_3RR) has more potential in NH_3 synthesis. Furthermore, NO_3^- exhibits higher solubility in aqueous solutions than N_2, providing the foundation for scalable and efficient production of NH_3.[12,13] Simultaneously, the extensive application of nitrate fertilizers to boost crop growth, along with animal manure, particularly from intensive livestock farming, excessive irrigation on agricultural lands, decomposition of crop residues in soil, and activities like mining, explosives manufacturing, and fertilizer industries, lead to the accumulation of nitrates in water bodies, posing a significant threat to human health.[14–18] In this context, the NO_3RR not only produces high-value, zero-carbon hydrogen-rich fuel but also effectively removes NO_3^- pollutants from water bodies, which mitigates energy crises and environmental pollution, offering broad and crucial prospects for application.

However, the NO_3RR is a complex reaction involving proton-coupled electron transfer (PCET).[19,20] A series of essential steps are interconnected in a sequential manner:[21] (a) the NO_3^- migrates to the catalyst surface. (b) The electrons successively transfer to the active sites to participate in the catalytic process. (c) Active sites facilitate the adsorption and activation of NO_3^-, the intermediate conversion, and NH_3 desorption. The primary challenge in achieving high-performance catalysis lies in the sluggish reaction kinetics induced by restricted mass transfer, complex multi-electron and proton transfer processes, and inappropriate adsorption/desorption of NO_3^- and intermediates, leading to poor activity for NH_3 production and severe competing hydrogen evolution reactions.[22–24] Based on this, various strategies have been proposed, including controlling the nanostructure of the catalyst,[25,26] tandem catalysis,[27,28] introducing defects,[29,30] designing single/dual atoms,[31,32] and forming alloys.[33,34] Besides, constructing a built-in electric field is vital in optimizing the adsorption and desorption processes of reactants and intermediates.[21,35] A composite catalyst leads to the spontaneous electron transfer resulting from the various work functions of different components, thereby establishing a built-in electric field.[36] This strategy regulates the electronic distribution on the catalyst surface, thereby enhancing its intrinsic activity. Additionally, adjusting the coordination environment of active sites and modulating the catalyst-electrolyte electrical double layer can effectively introduce an electric field.[37,38] Besides constructing a built-in electric field, introducing external stimuli can effectively regulate the thermodynamic and kinetic performance of the NO_3RR. For instance, renewable solar energy can stimulate catalysts possessing localized surface plasmon resonance (LSPR) effects to generate high-energy hot electrons and an intense electric field, thereby promoting the NO_3RR.[39] The introduction of a built-in electric field and external stimuli has been proven to facilitate the NO_3RR to produce NH_3. However, a comprehensive summary and in-depth understanding of strategies involving built-in electric field/external stimuli for the NO_3RR are deficient.

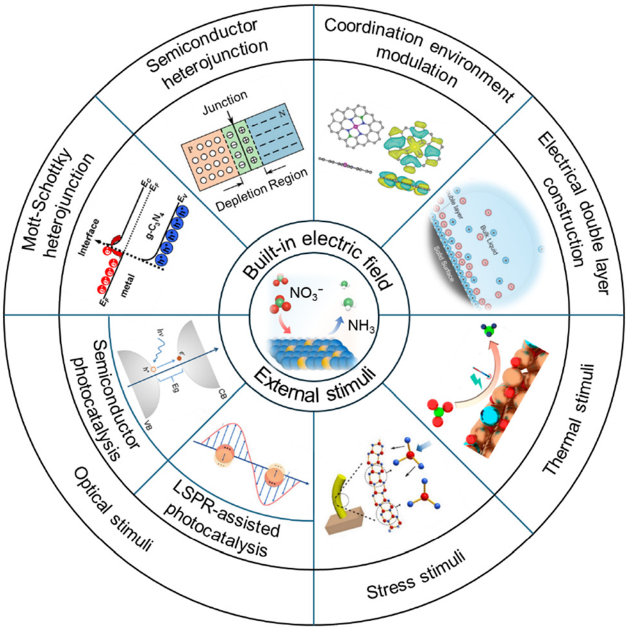

Fig. 1 Schematic of a built-in electric field/external stimuli-assisted NO_3RR.

In this review, we thoroughly summarized various strategies involving a built-in electric field/external stimuli in enhancing the NO_3RR and analyzed their mechanisms (Fig. 1). The aim is to provide insights into such modulation strategies for NO_3^- reduction to produce NH_3. This paper begins by introducing the fundamental principles and challenges of the NO_3RR, then reviews strategies for introducing a built-in electric field through constructing Schottky heterojunctions, semiconductor–semiconductor heterojunctions, adjusting active site coordination environments, and modulating electrical double layers in promoting the NO_3RR. Additionally, we summarize the effects of various external stimuli, including light, stress, and thermal, on NH_3 production. Finally, we emphasize the challenges and perspectives of modulation strategies from the built-in electric field or external stimuli to enhance the NO_3RR.

2. Fundamentals of NH_3 synthesis

2.1. Mechanism of the NO_3RR

Diverse reaction intermediates and products can be obtained in the NO_3RR involving various pathways because of the wide range of nitrogen's oxidation states (−3 to +5).[40] The NO_3^- concentration and pH value of the electrolyte closely influence the mechanism in the NO_3RR.[41] The NO_3RR can be broadly categorized into indirect and direct reduction processes. The indirect reduction process involves intermolecular self-catalysis to generate active species, typically occurring in high NO_3^- concentrations (>1 mol L^{-1}) in acidic electrolytes. Current research mainly centers on the direct reduction process, which includes electron-mediated and hydrogen atom-mediated reductions (Fig. 2).[42]

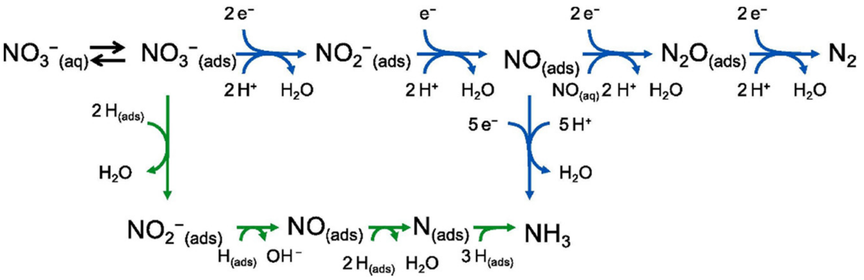

Fig. 2 The electron-mediated (blue arrow) and hydrogen atom-mediated (green arrow) pathways of the NO_3RR. Reproduced with permission.[42] Copyright 2021, Elsevier B.V.

In electron transfer-mediated NO_3RRs, various products can be generated through the reaction, including NO_2, NO_2^-, NO, N_2O, N_2, NH_2OH, and NH_3. Notably, N_2 and NH_3 are primary products owing to their high thermodynamic stability.[43] In this process, NO_3^- is firstly adsorbed onto the active sites of the catalyst (eqn (1.1)).[44] The subsequent reduction of NO_3^- to NO_2^- is usually considered the rate-determining step (RDS) in the NO_3RR (eqn (1.2)).[45] Thus, the NO_3RR performance is affected by the concentration of NO_3^-. In the electrolyte with low NO_3^- concentrations, the reaction process is influenced by co-adsorbed ions, whereas in cases of high NO_3^- concentrations, the active site density of the catalyst becomes the pivotal factor.[41] The intermediate NO_2^- demonstrates obvious reactivity on the catalyst, leading to adsorbed NO (eqn (1.3)), significantly determining product distribution.[46] $NO_{(ads)}$ can either undergo reduction to NH_4^+ (eqn (1.4)), serving as the final product or desorb from the active sites to produce NO in the electrolyte (eqn (1.5)).[47] The NO dimers with weak adsorption are formed in the presence of $NO_{(aq)}$ in the electrolyte, serving as precursors for N_2O (eqn (1.6)), which is subsequently reduced to N_2 (eqn (1.7)).[48–51]

$$NO_{3(aq)}^- \rightleftarrows NO_{3(ads)}^- \tag{1.1}$$

$$NO_{3(ads)}^- + 2H^+ + 2e^- \rightarrow NO_{2(ads)}^- + H_2O \tag{1.2}$$

$$NO_{2(ads)}^- + 2H^+ + e^- \rightarrow NO_{(ads)} + H_2O \tag{1.3}$$

$$NO_{(ads)} + 6H^+ + 5e^- \rightarrow NH_4^+ + H_2O \tag{1.4}$$

$$NO_{(ads)} \rightarrow NO_{(aq)} \tag{1.5}$$

$$NO_{(ads)} + NO_{(aq)} + 2H^+ + 2e^- \rightarrow N_2O_{(ads)} + H_2O \tag{1.6}$$

$$N_2O_{(ads)} + 2H^+ + 2e^- \rightarrow N_2 + H_2O \tag{1.7}$$

Meanwhile, NO_3RRs can also occur following the hydrogen atom ($H_{(ads)}$)-mediated reduction process. The Volmer step of water dissociation provides $H_{(ads)}$ as shown in eqn (1.8).[52,53] Atomic hydrogen (H) is a potent reducing agent ($E^\circ(H^+/H) = -2.31$ V *vs.* SHE),[54] which can reduce NO_3^-, NO_2^-, and NO adsorbed on the active sites (eqn (1.9)–(1.11)).[55] Kinetically, the formation of N–H bonds occurs more readily than the formation of N–N bonds, resulting in NH_3 being the primary product of this pathway (eqn (1.12)–(1.14)).[56,57]

$$H_2O + e^- \rightarrow H_{(ads)} + OH^- \quad \text{(Volmer)} \tag{1.8}$$

$$NO_{3(ads)}^- + 2H_{(ads)} \rightarrow NO_{2(ads)}^- + H_2O \tag{1.9}$$

$$NO_{2(ads)}^- + H_{(ads)} \rightarrow NO_{(ads)} + OH^- \tag{1.10}$$

$$NO_{(ads)} + 2H_{(ads)} \rightarrow N_{(ads)} + H_2O \tag{1.11}$$

$$N_{(ads)} + H_{(ads)} \rightarrow NH_{(ads)} \tag{1.12}$$

$$NH_{(ads)} + H_{(ads)} \rightarrow NH_{2(ads)} \tag{1.13}$$

$$NH_{2(ads)} + H_{(ads)} \rightarrow NH_{3(ads)} \tag{1.14}$$

The $H_{(ads)}$-mediated NO_3RR generally occurs at low overpotentials, which is essential for inhibiting side reactions. This pathway is particularly advantageous in noble metal catalysts, owing to their strong affinity for hydrogen.[58] Conversely, the electron transfer pathway is more probable on catalysts that exhibit a high adsorption capacity for NO_3^-.

2.2. Challenges and dilemmas in the NO_3RR

The NO_3RR occurs at the solid–liquid interface, presenting a lower reaction barrier than the solid–gas–liquid interface associated with the NRR. However, thermodynamically, the overpotential for NH_3 production is similar to that of several byproducts, such as N_2O (1.12 V *vs.* RHE), NO (0.96 V *vs.* RHE), and NH_2OH (0.73 V *vs.* RHE).[59] Additionally, to achieve higher NH_3 yield rates, it may be necessary to apply more negative electrode potentials, but this can simultaneously promote the competitive HER and reduce the faradaic efficiency of NH_3 production, leading to unsatisfactory energy efficiency in the NO_3RR.[2,31,53,60,61] Furthermore, from a kinetic perspective, the NO_3RR pathway for NH_3 generation is complex, involving an eight-electron and nine-proton transfer process, resulting in sluggish kinetics.[62] Consequently, developing catalysts for the NO_3RR that achieve high NH_3 yield rates and selectivity remains a significant challenge.

Meanwhile, the necessary overpotential for the NO_3RR and the source of protons depend on the pH of the electrolyte. Under acidic conditions, protons come from H^+, leading to the following reaction equation:

Overall reaction:

$$NO_3^- + 4e^- + 5H^+ \rightarrow NH_3 + O_2 + H_2O \tag{1.15}$$

Cathode:

$$NO_3^- + 8e^- + 9H^+ \rightarrow NH_3 + 3H_2O \quad (E_0 = 0.88\text{ V}) \tag{1.16}$$

Anode:

$$2H_2O \rightarrow O_2 + 4H^+ + 4e^- \quad (1.17)$$

Under neutral and alkaline conditions, H_2O acts as the source of protons, resulting in the following reaction equation:

Overall reaction:

$$NO_3^- + 2H_2O \rightarrow NH_3 + 2O_2 + OH^- \quad (1.18)$$

Cathode:

$$NO_3^- + 8e^- + 6H_2O \rightarrow NH_3 + 9OH^- \quad (E_0 = 0.69\ V) \quad (1.19)$$

Anode:

$$8OH^- \rightarrow 2O_2 + 4H_2O + 8e^- \quad (1.20)$$

The information above indicates that the reduction potential (E_0) for the NO_3RR is lower under acidic conditions (0.88 V) compared to alkaline electrolytes (0.69 V), resulting in more favorable thermodynamics.[63,64] Nevertheless, under acidic conditions, the intense competition for hydrogen adsorption on the active sites impedes the NO_3RR process. While NH_3 synthesis costs in alkaline environments are already below the commercial price,[2] the slow mass transfer requires higher voltages to achieve substantial yields, leading to increased energy consumption. This challenge is particularly pronounced in neutral media.

The activity and selectivity of the NO_3RR are influenced by different factors, including the NO_3^- concentration, catalyst type, and diffusion dynamics. For a specific catalyst, enhancing the mass transfer can significantly improve the NO_3RR. Increasing the concentration of NO_3^- enhances the accessibility of active sites to NO_3^-, thereby accelerating the reduction reaction. However, as the reaction progresses, the concentration of NO_3^- in the electrolyte diminishes, resulting in a gradual decrease in the NH_3 yield rate. It is also crucial to understand whether the decrease in NH_3 yield rate is related to catalyst deactivation or is simply due to a reduction in reactant concentration. Nevertheless, addressing mass transfer limitations in the NO_3RR requires different strategies to those in CO/CO_2 reduction reactions.[65,66] To alleviate the limitations of mass diffusion issues in the CO/CO_2 reduction reaction, gas diffusion electrodes can be utilized in flow-cell reactors to directly provide gaseous reactants to the electrolyte/electrode interface, which is not applicable to the NO_3RR because NO_3^- is dissolved in the electrolyte.[67] Consequently, developing methods to enhance the mass transport of NO_3^- under different conditions remains a significant challenge for future research.

Based on the mechanism and the challenges in the NO_3RR, proposing a well-designed strategy to regulate the adsorption and activation of NO_3^- at active sites, control the transfer behavior of electrons and active hydrogen to suppress side reactions and facilitate the hydrogenation process, and manage mass diffusion to ensure a sufficient supply of reactants is essential for achieving high activity and selectivity for NH_3 production *via* NO_3RRs. The strategy not only enhances the efficiency of the reaction but also provides a pathway for the industrial application of the NO_3RR.

3. NH_3 synthesis enhanced by built-in electric fields

Enhancing NH_3 synthesis through manipulating built-in electric fields represents a promising avenue in catalysis.[68–72] These fields can profoundly impact the energies of key reaction steps, ultimately influencing the catalytic process. Researchers can fine-tune the adsorption energies of reactants and intermediates by designing these fields within catalysts, thereby steering the reaction towards more favorable pathways. This approach can boost the catalytic activity and facilitate the selectivity of the NH_3 synthesis reaction, offering a pathway towards more sustainable and efficient NO_3RRs.

3.1. Mott–Schottky heterojunction

Utilizing the difference in work functions between metals and semiconductors to construct a Mott–Schottky heterojunction is an effective strategy for introducing a built-in electric field.[73] When a metal and a semiconductor come into contact to form a rectifying junction, the energy bands of the semiconductor bend to match the work function (Φ) of the metal, triggering electrons to transfer from the component of lower work function to that with a higher work function, ultimately resulting in the alignment of the Fermi levels of both components.[74] In detail, as shown in Fig. 3a, when the metal's work function is greater than that of the semiconductor, electrons irreversibly transfer towards the metal upon contact, leading to electron accumulation on the metal side and depletion on the semiconductor side at the interface, resulting in an upward bending of the semiconductor's conduction and valence bands at the interface, forming an intrinsic electric field.[75] Conversely, when the metal's work function is lower than that of the semiconductor (Fig. 3b), electrons migrate irreversibly toward the semiconductor until the Fermi levels of both materials align. This process leads to electron accumulation on the semiconductor side and depletion on the metal side at the interface, resulting in a downward bending of the semiconductor's conduction and valence bands at the interface, thereby establishing a built-in electric field.[73] Based on the mechanism mentioned above, the charge distribution state and the built-in electric field on the metal–semiconductor contact interface can be controlled by constructing different Mott–Schottky heterojunctions, potentially regulating the transfer of electrons in catalytic reaction processes and significantly altering the adsorption and desorption of specific reactants. Therefore, the development of Mott–Schottky heterojunction catalysts presents a strategy conducive to enhancing performance in the synthesis of NH_3.

To introduce the electric field induced by the Schottky barrier for promoting NH_3 production, Li and colleagues[76] fabricated electron-deficient Ni nanoparticles within nitrogen-rich carbon matrices (Ni_x/NC-sd). Computational simulations showed that the localized electric field at the charged electrodes can significantly enhance the density of NO_x^- ions (Fig. 3c), thereby accelerating the reduction process. This strategy facilitates the capture activation of NO_x^- and leads to high catalytic efficiencies for NH_3 synthesis across a wide range of NO_x^- concentrations, maintaining a faradaic efficiency exceeding 95% in NH_3 production and

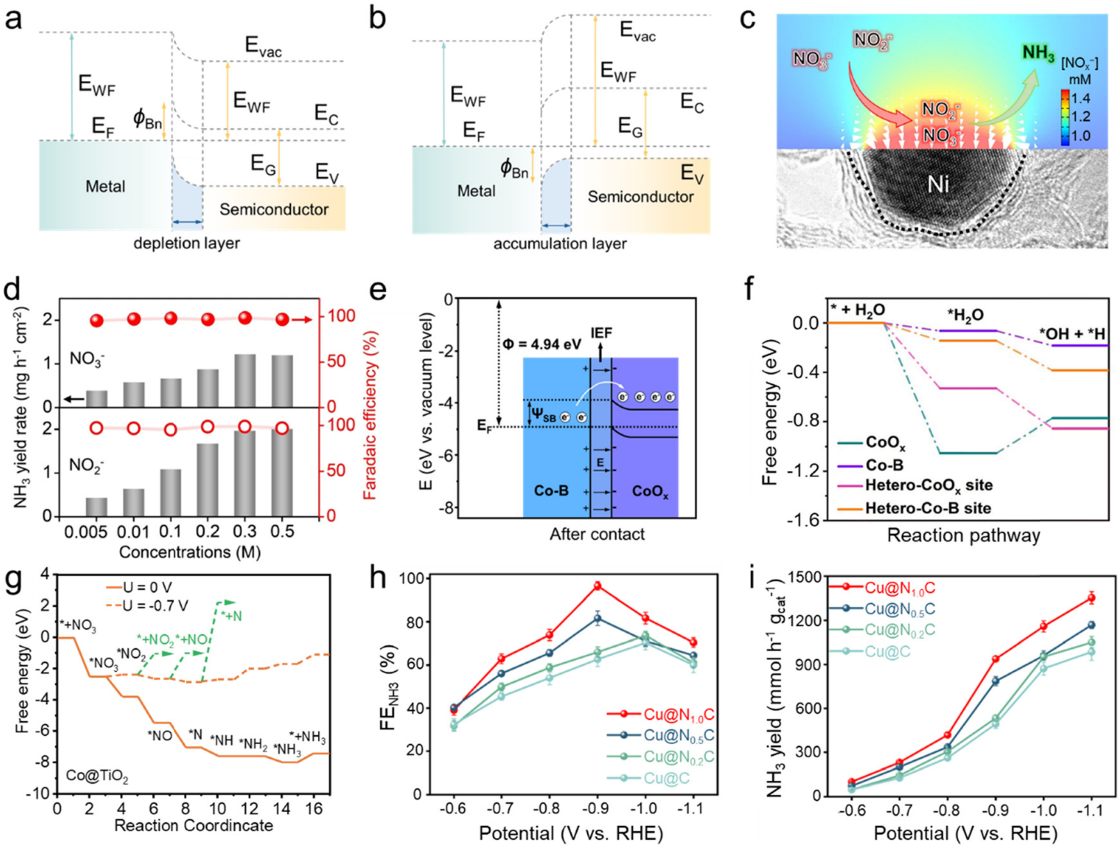

Fig. 3 (a) and (b) Energy band diagrams. E_{vac}, vacuum level; E_G, energy gap; E_{WF}, work function; E_c, conduction band edge; E_V, valence band edge; E_F, Fermi energy; ϕ_{Bn}, Schottky barrier. (c) The distribution of NO_x^- anions on the surface of Ni_x/NC-sd. The size and orientation of each arrow indicate the density and location of NO_x^- anions. The lower part of the image shows a high-resolution transmission electron microscopy image of Ni_x/NC-sd. (d) NH_3 yield rate and faradaic efficiency of Ni_{35}/NC-sd in 0.5 M Na_2SO_4 electrolyte with various NO_x^- concentrations at −0.5 V *vs.* RHE. Reproduced with permission.[76] Copyright 2021, Wiley-VCH. (e) Energy band diagrams of Co–B, and CoO_x after contact. E_F, Fermi energy; IEF, built-in electric field; Ψ_{SB}: Schottky barrier. (f) Free energy diagrams of H_2O dissociation on different sites. Reproduced with permission.[36] Copyright 2024, Royal Society of Chemistry. (g) Free energy diagram of $Co@TiO_2$ adsorbing different intermediates in the NO_3RR. Reproduced with permission.[77] Copyright 2023, Wiley-VCH. (h) Faradaic efficiency and (i) yield rate of NH_3 for Cu@N_xC obtained in 0.5 M Na_2SO_4 and 0.1 M $NaNO_3$. Reproduced with permission.[78] Copyright 2024, Royal Society of Chemistry.

achieving a NH_3 yield rate of 5.1 mg h^{-1} cm^{-2} from NO_3^- reduction and 25.1 mg h^{-1} cm^{-2} from NO_2^- reduction at −0.5 V *vs.* RHE (Fig. 3d). The remarkable NH_3 production performance can be reproduced over 5 consecutive cycling tests, indicating its robust stability. The work by Wang *et al.*[36] further evidenced the effectiveness of Mott–Schottky heterojunctions in enhancing NH_3 production performance. Based on the work functions and band energies of metallic Co–B and p-type semiconductive CoO_x, the formation of the Schottky contact in Co–B@CoO_x results in charge redistribution and the establishment of a built-in electric field (Fig. 3e). This phenomenon regulates the adsorption behavior of reactants and intermediates during the NO_3^- reduction to NH_3 process. Additionally, as protons derived from H_2O serve as essential reactants in the NH_3 production process, their research also demonstrates the influence of Schottky junction-induced electron redistribution on the behavior of H_2O molecules. As illustrated in Fig. 3f, Co–B@CoO_x exhibits enhanced capabilities in H_2O molecule adsorption and dissociation compared to counterparts, thereby facilitating proton provision for participation in the hydrogenation process. Zheng and colleagues[77] fabricated a Mott–Schottky heterojunction by loading Co nanoparticles onto TiO_2 nanobelt arrays and demonstrated the promoting effect of the built-in electric field on the NO_3RR by DFT calculations. The Schottky contact can mediate the electronic structure of $Co@TiO_2$, increasing the electron density on the surface of Co, which facilitates the adsorption of NO_3^-, thereby enhancing the reduction process. The free energy diagram of $Co@TiO_2$ adsorbing various species at different potentials in Fig. 3g exhibited the rate-determining step, *NH to $*NH_2$, was only 0.69 eV. Meanwhile, the calculated free energy, which discourages the generation of NO_2, NO, and N_2, validates that the Schottky junction enhances the selectivity of the NH_3 production catalytic process. In addition to directly utilizing the built-in electric field of Schottky junctions to regulate the adsorption of reactants and intermediates, Yu and his colleagues[78] also employed Schottky junctions to promote the NO_3RR by adjusting the state of active sites. They uniformly dispersed Cu nanoparticles on N-doped carbon substrates, where the N doping adjusted the carbon bandgap and regulated Mott–Schottky heterostructures. Due to the Schottky contact, electrons transferred irreversibly from Cu to the substrate, forming a built-in electric field and converting Cu sites into electron-deficient states, increasing the Cu^+ concentration. This adjustment facilitated the activation and adsorption of NO_3^-, resulting in a faradaic efficiency for NH_3 production of 96.2% at −0.9 V *vs.* RHE (Fig. 3h), along with an NH_3 yield rate of 1353.1 mmol h^{-1} g_{cat}^{-1} at −1.1 V *vs.* RHE (Fig. 3i).

3.2. Semiconductor–semiconductor heterojunction

A semiconductor heterojunction is a structure composed of different types of semiconductor materials, mainly categorized as p–n and non-p–n junctions. Taking the p–n junction as an example (Fig. 4a), when p-type and n-type semiconductors come into contact, a built-in electric field is formed at the interface due to the diffusion of electrons and holes. This electric field effectively separates electrons and holes and inhibits their recombination, prolonging the lifetime of charges. Additionally, this unique structure allows for spatial separation of oxidation–reduction sites. To utilize the distinctive properties of semiconductor heterojunctions for NO_3RR, Lu and colleagues[35] developed a novel electrocatalyst by layering CuCl (111) and rutile TiO_2 (110) with distinct work functions. The electron transfer from TiO_2 to CuCl leads to a built-in electric field (BEF), and is hence named CuCl_BEF. They utilized molecular dynamics simulation in the electrolyte containing 100 mg L^{-1} NO_3^- and concluded that after 10 ns, the peak concentration of NO_3^- positioned on the CuCl_BEF side reached 12.3 ions per nm^3, surpassing the concentration observed on the pure CuCl surface (6.3 ions per nm^3, as shown in Fig. 4b). Consequently, NO_3^- with ultra-low concentrations (100 mg L^{-1}) was converted to NH_3 at a remarkable production rate of 1.82 mg h^{-1} cm^{-2} (Fig. 4c). In contrast, CuCl + MXene without a built-in electric field exhibited a lower rate. The CuCl_BEF catalyst displayed negligible fluctuations in selectivity during consecutive recycling tests, indicating its superior stability (Fig. 4d). The theoretical calculation shows that the electric field facilitated the accumulation of NO_3^- ions on the catalyst surface, enhancing the reaction rate and lowering the energy

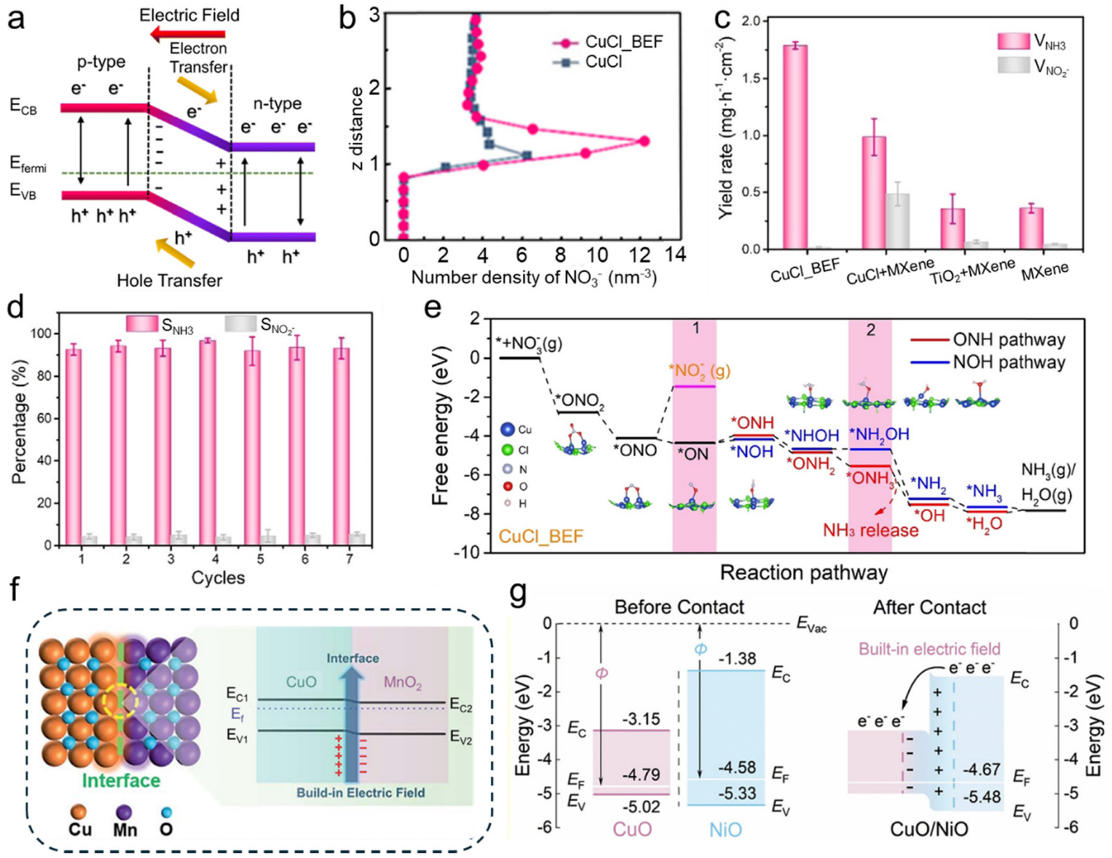

Fig. 4 (a) Schematic demonstrating the band structure and built-in electric field formation mechanisms in the p–n heterojunction. Reproduced with permission.[79] Copyright 2024, Royal Society of Chemistry. (b) Spatial distribution of NO_3^- on the catalyst surface obtained from molecular dynamics simulation. CuCl_BEF represents a heterojunction composed of CuCl and TiO_2 with an induced built-in electric field. (c) Average NH_3 yield rate over 6 h for various electrocatalysts. (d) Consecutive recycling tests at −1.0 V *vs.* RHE for CuCl_BEF. (e) Free energy diagram of reaction pathways for reducing NO_3^- to NH_3 on the CuCl_BEF. Reproduced with permission. Copyright 2021, Wiley-VCH. (f) Schematic presenting the band structures and built-in electric field formation of CuO/MnO_2. Reproduced with permission.[80] Copyright 2022, Royal Society of Chemistry. (g) Band structures of CuO and NiO pre-contact (left) and post-contact (right). Reproduced with permission.[69] Copyright 2024, Elsevier B.V.

barrier of the RDS for the key reaction intermediate *NO (Fig. 4e). The presence of the electric field in this semiconductor heterojunction can enhance ion adsorption, thereby boosting catalytic efficiency. This strategy suggests new avenues for designing innovative catalysts tailored for reactions involving ions as reactants.

Meanwhile, Wang and colleagues[80] developed a novel hierarchical structure of CuO@MnO_2 1D core–2D shell nanoarrays supported on a Cu foam substrate (CuO@MnO_2/CF). Integrating MnO_2 nanosheets onto the CuO nanowire arrays offers a high density of active sites and enhances mass transfer. Notably, the CuO/MnO_2 heterojunction establishes an built-in electric field at the interface, promoting the accumulation of NO_3^- and expediting NO_3^- reduction kinetics through optimized adsorption processes (Fig. 4f). As a result, the CuO@MnO_2/CF composite demonstrates an exceptional NH_3 faradaic efficiency of 94.92%, remarkable NH_3 selectivity of 96.67%, and superior NO_3^- conversion of 99.38% in the NO_3RR. In another study, benefiting from the superior H_2O-to-H* conversion capabilities of nickel-based semiconductors,[81,82] Zou and co-workers[69] created a heterojunction by combining CuO and NiO due to their matched work functions. Through analyses using X-ray photoelectron spectroscopy (XPS) and ultraviolet photoemission spectroscopy (UPS), a semiconductor–semiconductor heterojunction between CuO and NiO was validated, which can trigger a built-in electric field. The catalytic performance of CuO/NiO in the NO_3RR under low NO_3^- concentrations including NO_3^- conversion rates, product selectivity (NH_4^+, NO_2^-, and N_2), and faradaic efficiency, was assessed by comparing with the performance of pure CuO and NiO. The influence of applied potentials, pH of the electrolyte, and NO_3^- concentrations on the catalytic performance of CuO/NiO in the NO_3RR was also investigated. Density functional theory (DFT) calculations revealed that the CuO/NiO system, with its built-in electric field, is conducive to enhancing reactant mass transfer and H* provision. Based on the experimental and theoretical results, they summarized the origination of the promotion of CuO/NiO in the NO_3RR. As illustrated in Fig. 4g, upon the contact between CuO and NiO, the spontaneous electron flow leads to band bending, creating a built-in electric field that accelerates charge transfer and the rate of the NO_3RR.

3.3. Coordination-environment modulation

In addition to heterojunction interfaces, introducing an electric field by adjusting the coordination environment of catalysts can also enhance catalytic processes. The coordination structure near active sites can effectively influence electron distribution and induce built-in electric fields, thereby modulating the adsorption behavior of reactants and intermediates. Moreover, it has been demonstrated that modulating the built-in electric field between dual-layer single-atom catalysts can also effectively adjust polarization, suppressing competitive reactions in the NO_3RR.[37]

Frauenheim and colleagues[37] proposed a universal strategy of heterogeneous bilayer single-atom catalysts with tunable surface chemistry to enhance the NO_3RR. The asymmetric atomic design of these catalysts leads to a dipole moment that can strengthen built-in electric fields, regulating the activation of reactants and the adsorption of intermediates, thus modulating reaction pathways and enhancing NH_3 selectivity and activity. They investigated a series of bilayer N-doped graphene (GN) supported single-atom catalysts. High-throughput calculations revealed that TiV-N_4, NbV-N_4, and GaV-N_4-G_N can all suppress competitive HERs with favorable limiting potentials of −0.32, −0.20, and −0.25 V, respectively. In the free energy diagrams of V_2-N_4-G_N (Fig. 5a), apart from the $*NO_3^- \rightarrow *NO_3H$ and $*NO \rightarrow *NOH$ steps showing an upward ΔG, the remaining hydrogenation processes exhibit a downward ΔG. NH_3 desorbs from the adsorption site after overcoming a small final free energy barrier of 0.1 eV, indicating fast NH_3 desorption from the catalyst surface. Therefore, the rate-determining step in this system is the $*NO \rightarrow *NOH$ transformation. The authors also summarized the limiting potential and RDS of the NO_3RR on MV-N_4-G_N (Fig. 5b), indicating a strong dependence of the RDS and limiting potential on polarization. Compared to the upward ΔG for $*NO_3^- \rightarrow *NO_3H$ in V_2-N_4-G_N, the corresponding step in NbV-N_4-G_N shows a downward ΔG (Fig. 5c). Furthermore, in the subsequent hydrogenation steps, polarization did not alter the most stable NO adsorption mode and the most favorable adsorption pathway for the NO_3RR. Instead, the RDS shifted to the desorption of NH_3 from the surface.

Polarization can adjust the strength of interactions between intermediates and catalysts, thereby influencing the selectivity of reactions. Consequently, the limiting potential of byproducts was calculated to investigate the ease of byproduct formation on NbV-N_4-G_N. For most MV-N_4-G_N catalysts (excluding ZrV, MgV, and CaV, as shown in Fig. 5d), the ΔG_{*H} values are significantly higher than those of the NO_3RR, indicating that MV-N_4-G_N retains its inhibitory effect on the HER. Therefore, the unique atomic structure and electronic properties of heterogeneous BSACs contribute to the polarization dependence and controllable selectivity of the NO_3RR. Furthermore, the volcano-shaped relationship between the limiting potentials (U_L) and adsorption free energy of NO_3^- (ΔG_{*NO_3}) indicates that heterogeneous BSACs exhibit a higher activity compared to their counterparts (Fig. 5e). The plane-average potential of NbV-N_4-G_N in Fig. 5f further confirms the existence of an electric field and that can be modulated through substituting other atoms. As shown in Fig. 5g and h, after Nb substitution, the color deepens around the V atom, indicating an enhanced electric field around V, further validating the feasibility of regulating the coordination environment to enhance the electric field. Therefore, the built-in electric field in BSACs can promote the accumulation of NO_3^- and mass transfer on the surface of the catalyst for an improved NO_3RR (Fig. 5i). Meanwhile, Zhao and co-workers[83] doped boron into carbon substrate to adjust the coordination structure of Ni SACs and construct B–N bonds to trigger the electric field that could facilitate the adsorption of NO_3^-. Compared to the catalyst without an electric field, that is, without doping boron, the faradaic efficiency of NiSA@BNG increased to ≈95% from 51% and the yield rate is 2 times higher. As shown in the density of states for NiSA@BNG, the B atoms significantly increase the density of states and redistribute the density of state (DOS; as shown in Fig. 5j and k), indicating the promoted

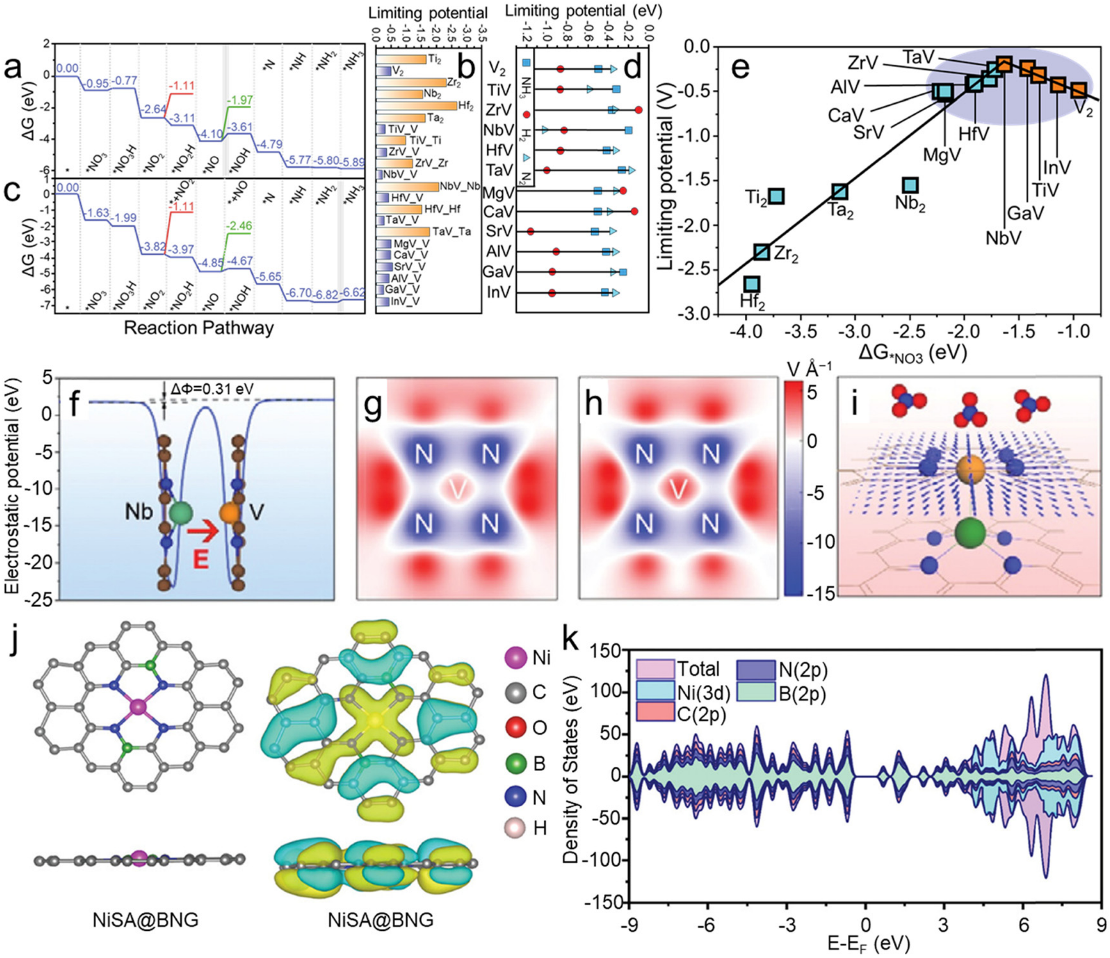

Fig. 5 Free energy diagram for the reduction of NO_3^- to NH_3 on (a) V_2-N_4-G_N and (c) NbV-N_4-G_N. (b) Limiting potentials on M_2-N_4-G_N and MV-N_4-G_N for the NO_3RR. (d) Limiting potentials for generating various products during the NO_3RR process. (e) Volcano-shaped relationship between U_L and ΔG_{*NO_3}. (f) Plane-averaged potential of NbV-N_4-G_N. The simulated electric field on (g) V_2-N_4-G_N and (h) NbV-N_4-G_N, in which the unit is V Å^{-1}. (i) Schematic depicting the electric field from NbV-N_4-G_N, with each arrow's size and direction indicating the field's strength and orientation. Reproduced with permission.[37] Copyright 2022, Wiley-VCH. (j) Optimized structures and charge distribution of NiSA@BNG. (k) The DOS for the NiSA@BNG catalyst. Reproduced with permission.[83] Copyright 2024, Wiley-VCH.

conductivity of NiSA@BNG. Meanwhile, NiSA@BNG demonstrates superior stability, as evidenced by no significant decrease in faradaic efficiency and yield rate over 5 consecutive recycling tests. In conclusion, the introduced electric field declines the reaction energy barrier, promotes the adsorption of NO_3^- and enhances the stabilization of the catalyst.

3.4. Electrical double layer construction

Due to the electrode–electrolyte interface being the site of catalytic processes, research on the electrical double layer formed when the electrode contacts the electrolyte is crucial. As shown in Fig. 6a, the electrical double layer comprises the inner Helmholtz layer, outer Helmholtz layer, and diffusion layer.[84] The type and concentration of solvated ions in the electrical double layer play a critical role in catalytic reactions, where cations in the electrolyte can stabilize negatively charged reaction intermediates through local electric field effects. In this context, Yu and colleagues[38] studied the NO_3RR performance by using bulk Cu as the cathode and adjusting the types and concentrations of alkali metal ions in the electrolyte. As shown in Fig. 6b, various alkali metal cations (Li^+, Na^+, K^+, Cs^+) were selected for COMSOL multi-physics simulations, and the resulting electric double layer (EDL) all exhibited negative potentials, which indicates the effectiveness of utilizing alkali metal cations in the electrolyte to modulate the electrolyte microenvironment within the EDL. This phenomenon can promote the dissociation of water molecules on the electrode surface and facilitate the rapid movement of generated OH^- away from the electrode surface towards regions of positive electrostatic potential (ESP). During this process, OH^- near alkali metal cations removed an H^+ from adjacent water molecules, thus facilitating proton transfer. The authors further compared the NO_3RR current obtained in electrolytes containing various alkali metal cations (Fig. 6c), with the current ordering as $K^+ > Na^+ > Li^+ \approx Cs^+$, consistent with the results shown in Fig. 6b. This alignment demonstrates that modulating the EDL effectively promotes the NO_3RR for NH_3 production. Adding Li^+, Na^+, and K^+ alkali metal cations had little effect on the potential-determining step, but introducing Cs^+ increased the reaction barrier of the potential-determining step, thereby inhibiting the NO_3RR (Fig. 6d).

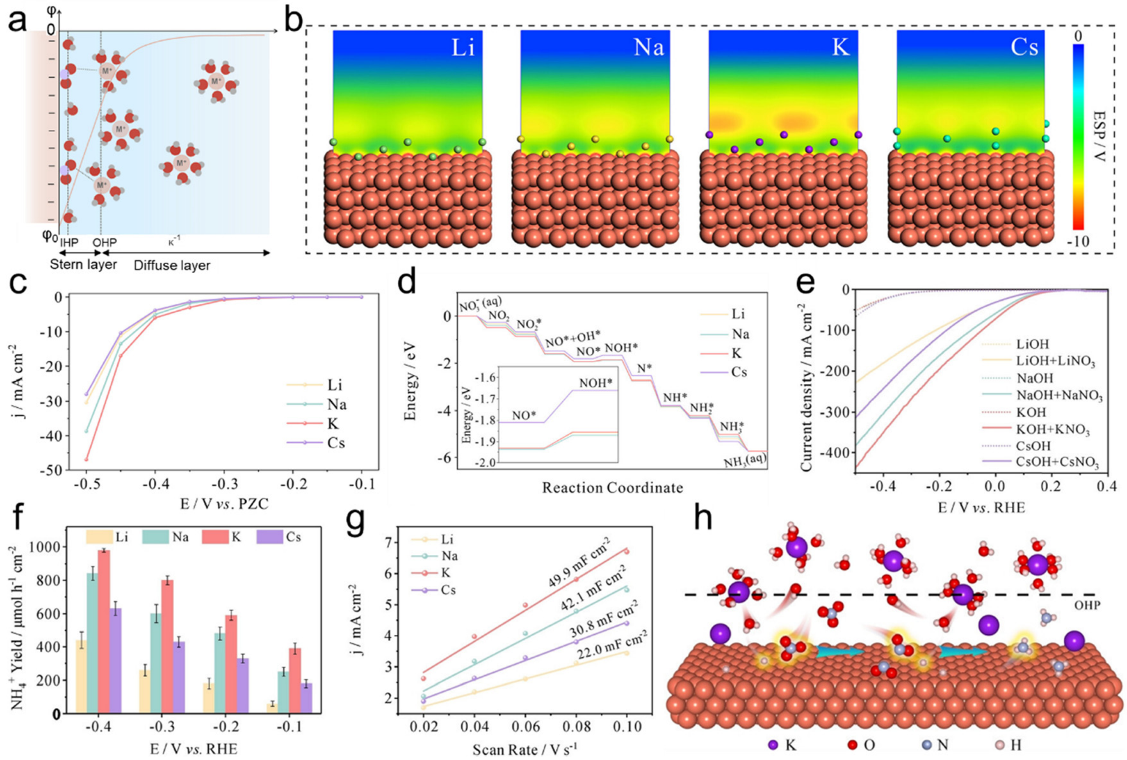

Fig. 6 (a) Schematic of the EDL. Reproduced with permission.[84] Copyright 2022, Elsevier B.V. (b) ESP distribution obtained from models with various alkali metal ions. (c) Simulated partial current densities of the NO_3RR using electrolytes with various alkali metal cations. PZC represents the potential of zero charge. (d) Free energy diagram for reducing NO_3^- to NH_3 with different alkali metal cations. (e) Linear sweep voltammetry (LSV) curves of Cu/Cu_2O in the electrolyte containing 1 M MOH and 1 M MOH + 0.05 M MNO_3. (f) NH_4^+ yield rate at different potentials in the electrolyte containing 1 M MOH and 0.05 M MNO_3 at 0.4 V *vs.* RHE. (g) Double-layer capacitance (C_{dl}) values in 1 M MOH with 0.05 M MNO_3. (h) Schematic diagram of the EDL-assisted NO_3RR process. Reproduced with permission.[38] Copyright 2024, Wiley-VCH.

The evaluation through electrochemical testing of the NO_3RR using Cu/Cu_2O with different alkali metal cations added to the electrolyte also assessed the promoting effect of local electric field effects on the reaction. In the presence of NO_3^-, the addition of various cations showed significant NO_3^- catalytic activity (Fig. 6e and f). The charge accumulation at the catalytic interface shows the most significant decrease in C_{dl} after adding K^+ (Fig. 6g). The conversion of NO_3^-, faradaic efficiency, selectivity for NH_4^+, and yield rate achieved 99%, 98%, 99.5%, and 980 μmol h^{-1} cm^{-2} in 1 M KOH, indicating the effectiveness of local electric field effects in promoting the reduction of NO_3^-. Combining the theoretical and experimental findings, a more comprehensive insight into the alkali metal cation-mediated strategy in the NO_3RR process was proposed (Fig. 6h). Alkali metal cations near the OHP regulate proton migration and impact the interactions between protons and intermediates. Among these cations, K^+ emerges as the most advantageous electrolyte component. It facilitates proton adsorption on the catalyst surface, promoting the hydrogenation process and enhancing the NO_3RR.

4. NH_3 synthesis enhanced by external stimuli

The reasonable design of external stimuli-assisted catalysis, that is, efficiently harnessing energy abundant on earth, including solar energy, thermal energy, and mechanical energy, has significant potential for producing renewable fuels and removing environmental pollutants. Recent studies have indicated that certain external stimuli, such as light and stress, can trigger the built-in electric field within the catalyst, effectively achieving charge separation and impacting catalytic activity, reaction kinetics, and selectivity in reducing NO_3^- to NH_3. Additionally, external stimuli can influence the catalytic reaction process through other pathways such as overcoming thermodynamic barriers in the NO_3RR. However, there is a lack of comprehensive summaries and an in-depth understanding of the research progress on the NO_3RR under different external stimuli.

4.1. Optical stimuli

Photocatalysis is a process that utilizes light energy to drive chemical reactions and is widely applied in pollutant removal and energy conversion.[85–87] It is primarily categorized into semiconductor photocatalysis and localized surface plasmon resonance (LSPR)-assisted photocatalysis. Semiconductor photocatalysis utilizes electron–hole pairs generated in semiconductor materials under light stimulation to catalyze reactions.[88,89] On the other hand, LSPR-assisted catalysis relies on the localized electric field enhancement effect and high-energy hot electrons and holes produced by metal nanoparticles under specific wavelength light, enhancing the efficiency of photocatalytic reactions.[90,91]

4.1.1 Semiconductor photocatalysis. Photocatalysis is an environmentally friendly technology using solar energy to facilitate chemical reactions. The photocatalyst, generally a semiconductor photocatalyst, plays a key role in photocatalysis.[92] The band theory serves as the theoretical basis for elucidating semiconductor photocatalysts. A solid is regarded as an infinite collection of atoms, each possessing the highest occupied molecular orbital (HOMO) and the lowest unoccupied molecular orbital (LUMO).[93] Atomic clusters can be described as combinations of atomic orbitals, resulting in closely spaced filled orbitals with higher energy and a set of closely spaced empty orbitals. As the size of the atomic clusters increases to an infinite collection, discrete energy levels decrease further, eventually forming energy bands. The band formed by the HOMO orbitals is called the valence band (VB), while the band formed by the LUMO orbitals is called the conduction band (CB). As shown in Fig. 7a,[94] the energy disparity between the VB and the CB is termed the band gap energy (E_g). When a photon carrying energy equal to or greater than E_g excites a semiconductor, it can elevate an electron from the VB to the CB.[95] The initial electron–hole pair formed is referred to as an exciton, held together by the electrostatic attraction between the opposite charges. After thermal relaxation, these charge carriers may recombine or migrate to the semiconductor's surface through non-radiative or radiative pathways. The positively charged holes with oxidation potential and the negatively charged electrons with reduction potential can participate in the redox of the reactant adsorbed on the active sites, constituting the semiconductor photocatalytic process. The band gap and the positions (potentials) of the VB and CB in a semiconductor play a crucial role in the light absorption capacity and the thermodynamics of the photocatalytic processes. Consequently, in the design of photocatalysts, it is essential to design both the VB and CB positions (representing oxidation–reduction potential) and the band gap (reflecting light absorption ability) of the semiconductor to satisfy the necessary conditions for the redox reactions.

Dong and co-workers[97] synthesized subnanometric alkaline-earth oxide clusters (MO_{NCs}, M = Mg, Ca, Sr or Ba) through the operando construction for NH_3 photosynthesis from NO_3^-. The electron paramagnetic resonance (EPR) measurements in Fig. 7b

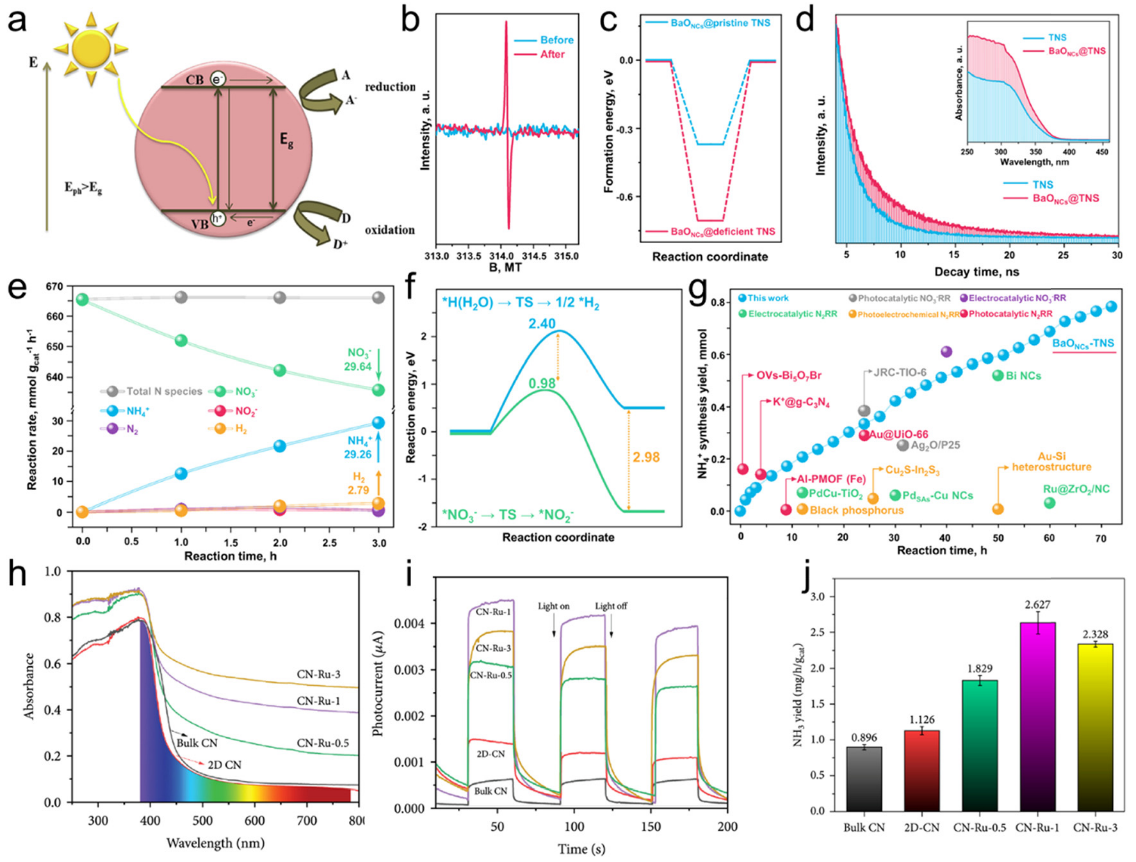

Fig. 7 (a) Schematic of semiconductor photocatalysis. Reproduced with permission.[96] Copyright 2020, Elsevier Ltd. (b) EPR results of TNS before and after introducing oxygen vacancies. (c) The formation energy of BaO_{NCs} loading on pristine and defected TNS. (d) Time-resolved fluorescence emission decay spectra. The inset is UV-vis DRS. (e) Reaction rate of various products in the NO_3RR. (f) Activation energy for NO_3^- reduction and H_2O dissociation. (g) Stability test of BaO_{NCs}-TNS and the performance comparison with other works. Reproduced with permission.[97] Copyright 2022, Springer Nature. (h) UV-Vis DRS and (i) photocurrent response of various samples. (j) Comparison of NH_3 yield rate by different catalysts. Reproduced with permission.[98] Copyright 2021, AAAS.

confirm the introduction of oxygen vacancies on TiO_2 nanosheets (TNS). DFT calculations (Fig. 7c) demonstrated the feasibility of uniformly depositing MO_{NCs} on photoinduced vacancies on TNS. Time-resolved fluorescence emission decay spectra in Fig. 7d revealed a significant enhancement in the charge separation capability of the composite structure. They employed ethylene glycol (EG) as the hole sacrificial agent. The oxidation of EG and the reduction of nitrate ions (NO_3^-) occur simultaneously, where the oxidation of EG consumes the holes that, in turn, can accelerate the NO_3RR, promoting NH_3 synthesis. As an essential parameter for evaluating performance in the NO_3RR, the selectivity of NH_3 production on BaO_{NCs}-TNS was investigated. As shown in Fig. 7e, 29.26 mmol g_{cat}^{-1} NH_4^+ was obtained after 3 h of photocatalysis. The total N species in the electrolyte during the catalyst remained stable, confirming the five-electron transfer process for N_2 generation was suppressed. The resulting selectivity for NH_3 production reached 97.67%. The activation energies for synthesizing NH_4^+ from NO_3^- and water splitting for H_2 production were determined through calculations (Fig. 7f). A significant reduction of 1.42 eV in activation energy was observed for the NO_3^- reduction reaction compared to water splitting, indicating the potential for effectively suppressing electron consumption in side reactions. A long-term stability test of BaO_{NCs}-TNS was carried out as shown in Fig. 7g, in which 0.78 mmol NH_4^+ was obtained after 72 h of photocatalysis, demonstrating leading-edge performance in the NO_3RR for NH_3 generation. Meanwhile, Ni and colleagues[98] loaded Ru on g-C_3N_4 in a photocatalyst for the NO_3RR. As shown in the UV-vis diffuse reflection spectra (DRS) of various samples (Fig. 7h), a significant redshift and improved light absorption in the visible light region were observed after Ru decorating on 2D-C_3N_4. The introduction of Ru facilities the separation of photogenerated electrons and holes, leading to an increased photo response (Fig. 7i). Benefiting from this strategy, the optimal catalyst displays a superior NH_3 yield rate of 2.627 mg h^{-1} g_{cat}^{-1}, 2.93 times higher than bulk g-C_3N_4 (Fig. 7j).

4.1.2 LSPR-assisted catalysis. When incident light strikes the surface of non-continuous metal nanostructures, such as metal nanoparticles, the electrons capable of oscillating freely within these structures efficiently absorb photons of similar frequencies in the incident light.[99–101] This absorption process takes place within the metal nanostructures, giving rise to the formation of surface plasmon resonance waves at the metal-dielectric interface. However, owing to the discontinuity of the nanostructures, the surface plasmon resonance waves are constrained to the immediate vicinity of the metal nanostructure's surface and cannot propagate indefinitely along the metal–dielectric interface. This phenomenon is known as localized surface plasmon resonance (LSPR).[102–104] Illustrated in the schematic of LSPR in Fig. 8a, in the case of spherical metal nanoparticles, when the electron cloud oscillates freely within the nanoparticles and absorbs the energy from incident photons, the high-energy electron cloud experiences a displacement from the nanoparticle's center.[105] Simultaneously, the Coulomb force between the metal atoms and the electrons induces a corresponding restoring force on the displaced electron cloud, leading to vigorous oscillations of the electron cloud near the metal atoms.[106] This excited oscillation of free electrons within the metal nanoparticles, triggered by incident light, can instigate the generation of LSPR within the metal nanoparticles through localized electric fields.

The effect generated on the surface of metal nanostructures can decay through relaxation processes, generating numerous hot electron–hole pairs.[109] Efficiently separating these hot electron–hole pairs shows promise for advancing catalytic processes like oxygen reduction, water splitting, methanol oxidation, and NH_3 synthesis.[110–113] Consequently, the effective separation and direct utilization of hot electron–hole pairs produced by the photoinduced metal LSPR effect, along with leveraging the improved catalytic activity and stability conferred by this effect, have captured considerable interest among researchers in the area of innovative sustainable and environmentally friendly energy research.

In LSPR-assisted NH_3 electrosynthesis, Jain and colleagues[39] synthesized Au nanoparticles with LSPR effects, serving as both photon-capturing materials and active sites for the NO_3RR. Their electrosynthesis and overall electrochemical activities were enhanced by a factor of 15 compared to traditional electrocatalysis (Fig. 8b–d), while the faradaic efficiency for NH_4^+ production increased from 71% to 76% (Fig. 8e). Additionally, they proposed that the enhancement of kinetics due to the LSPR effect is most pronounced near the onset potential under applied bias. At $\Delta E = -10$ mV, the LSPR effect boosted the NH_4^+ yield rate by 15 times, a level of activity that required an additional 140 mV of potential in the dark for the catalyst to achieve this (Fig. 8f). In conclusion, under light irradiation, the LSPR of Au nanoparticles is stimulated, generating electron–hole pairs through interband and intraband damping (Fig. 8g). High-energy electrons in the sp states drive the reduction of NO_3^- to NH_4^+, producing OH^-, while the holes are consumed by electrons in the circuit. This leads to an alkaline oxygen evolution reaction at the counter electrode, with the OH^- being oxidized.

Zhao and colleagues[108] utilized the internal electromagnetic field generated by Au NRs to synthesize Au NR@Cu_2O–AuPd NPs. The internal electromagnetic field (Fig. 8h) results from the distinct optical response properties of the bimetallic components and enhanced ability to adsorb NO_3^- and reaction intermediates, boosting the activity and selectivity in the NO_3RR. This led to an NH_3 yield rate of 4587.00 μg h^{-1} $mg_{cat.}^{-1}$ and a faradaic efficiency of 93.09% under neutral conditions (Fig. 8i and j).

4.2. Stress stimuli

Piezoelectricity is a fundamental material property that generates electric potential in response to stress stimuli. Typically, semiconductors exhibiting piezoelectric characteristics are polar materials possessing crystal structures that lack a center of symmetry. When subjected to stress, separating positive and negative charge centers within the lattice creates a piezoelectric potential on the material's surface. The most well-known piezoelectric materials, such as perovskite-structured Pb(Zr,Ti)O_3 (PZT), zinc oxide (ZnO), gallium nitride (GaN), and zinc sulfide (ZnS), are extensively utilized in diverse fields like mechanical

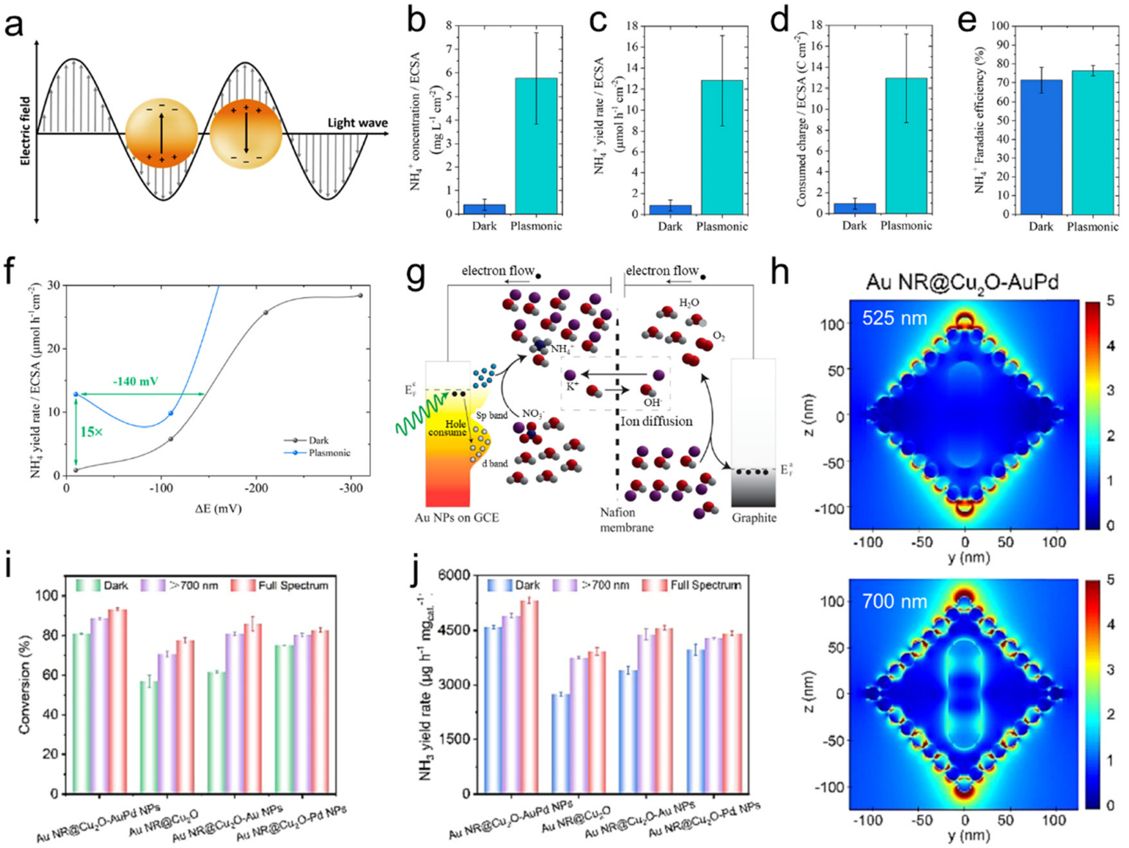

Fig. 8 (a) Schematic of LSPR. Reproduced with permission.[107] Copyright 2021, Springer Nature. (b) NH_4^+ concentration, (c) NH_4^+ yield rate, (d) consumed charge, and (e) NH_4^+ faradaic efficiency obtained in the dark and under 532 nm light irradiation. (f) NH_4^+ yield rate at various ΔE under different conditions. (g) Scheme of LSPR-assisted NH_4^+ electrosynthesis. The working electrode in (b)–(g) is Au nanoparticles on a glassy carbon electrode. Reproduced with permission.[39] Copyright 2022, American Chemical Society. (h) The finite-difference time-domain (FDTD) simulated electric-field distribution on Au NR@Cu_2O–AuPd NPs. (i) NO_3^- conversion rate and (j) NH_3 yield rate of different catalysts. Reproduced with permission.[108] Copyright 2024, Elsevier B.V.

energy harvesting, active sensing, and self-powered systems. This generated potential can facilitate the transfer of electrons and holes towards the material's surface, leading to the development of catalytic research based on the mechanical-to-chemical energy conversion using piezoelectric materials.[114]

The concept of piezoelectric catalysis is depicted in Fig. 9a. When subjected to external forces, piezoelectric materials generate an internal electric field because of spontaneous polarization. This electric field facilitates the separation of carriers towards the material's surface, thereby facilitating redox on the active sites. By adjusting external stress, such as controlling the frequency and power of the stress, both the orientation and strength of polarization can be manipulated. This dynamic regulation of surface properties has potential for the catalytic process. Research efforts have explored leveraging piezoelectric polarization to drive a series of catalytic processes, including water splitting, pollutant degradation, CO_2 adsorption/reduction, and the selective transformation of organic compounds.[115–118] In our previous work, we utilized the piezoelectric effect of the electron-rich $BaTiO_3$ (BTO-OV_1) to promote the catalytic performance of metal nanoparticles in the NO_3RR.[119] After introducing stress stimuli, the contact state between metal nanoparticles and the BTO-OV_1 substrate was modulated. The *I*–*V* curves in Fig. 9b go from curves to straight lines as the pressure increases, which confirms the contact state was from Schottky contact to ohmic contact. The DFT calculations further demonstrated that the stress stimuli adjusts the local electron distribution and promotes the interaction between metal nanoparticles and BTO-OV_1 (Fig. 9c). Based on the experimental and computational results, we proposed the mechanism of this strategy (Fig. 9d). After introducing stress stimuli, the contact state between metal nanoparticles and BTO-OV_1 was modulated due to the piezoelectric effect. Because of the difference in the work function, a large number of the electrons in BTO-OV_1 were transferred smoothly to the metal nanoparticles, which led to the generation of active hydrogen that participated in the hydrogeneration process in the NO_3RR. The charge transfer also triggers the charge redistribution, suppressing the Volmer–Heyrovsky step of the competing HER. The optimized catalyst displays a superior faradaic efficiency of 95.3% and a yield rate of 6.87 mg h^{-1} $mg_{cat.}^{-1}$ for NH_3 generation.

The piezoelectric polarization electric field triggered by stress stimuli also has the potential to assist photocatalysis. Chen and colleagues[120] synthesized a naphthalene-linked perylene diimide polymer (N-PDA) with rigidity and polarity for

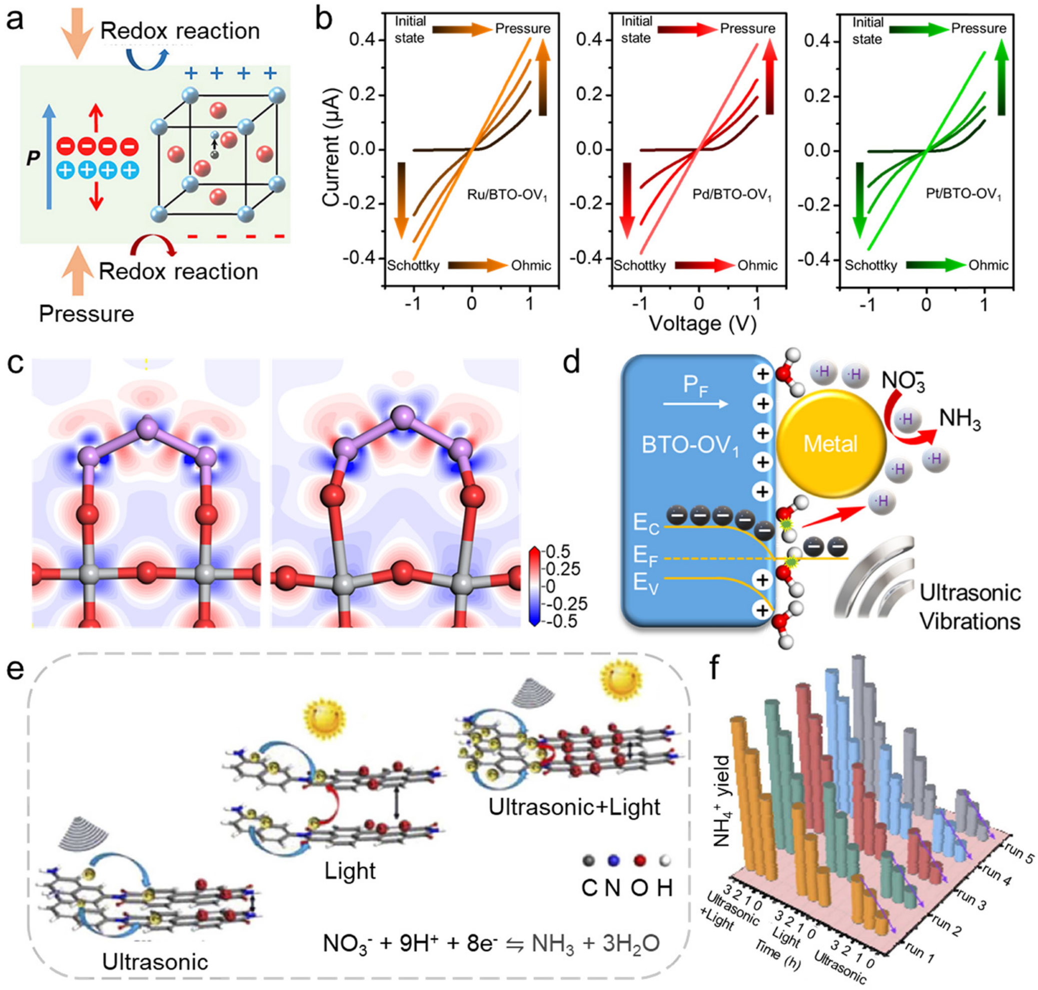

Fig. 9 (a) Schematic of the piezoelectric catalysis. Reproduced with permission.[115] Copyright 2020, American Chemical Society. (b) *I*–*V* curves measured at different pressure using M/BTO-OV_1 (M = Ru, Pd, and Pt). (c) Electron density difference mappings obtained from Ru/BTO-OV_1 without (left) and with pressure (right). (d) Schematic diagram of piezoelectric-assisted electrochemical NO_3RR. In (c) and (d), the red, gray, purple, and white balls represent O, Ti, Ru, and H atoms, respectively. Reproduced with permission.[119] Copyright 2023, Elsevier Ltd. (e) Schematic of charge transfer of N-PDA under various conditions. (f) NH_4^+ yield rate measured under different conditions. Reproduced with permission.[120] Copyright 2024, Elsevier B.V.

producing NH_3 from NO_3^-. The stress stimuli triggers the piezoelectric polarization electric field of the catalyst, further facilitating the separation of photogenerated charge carriers and suppressing their recombination (Fig. 9e). The NH_3 production rate through piezo-photocatalysis exceeded the sum of the yield rates obtained by piezoelectric catalysis and photocatalysis, further confirming the promotion of the stress stimuli in the NO_3RR (Fig. 9f).

4.3. Thermal stimuli

Thermal catalysis primarily involves heating to provide the energy needed for catalytic reaction systems to overcome thermodynamic barriers, thus driving the conversion of reactants into products.[121–124] In catalysis, electrons are typically driven and facilitated to transfer through electrical work under an applied voltage. Nevertheless, in steps except for electron transfer, the electric potential may not effectively influence the thermodynamics of the reaction. Introducing thermal stimuli offers a promising strategy for adjusting reaction thermodynamics, and the overpotential arising from kinetic barriers exceeding thermodynamic barriers can also be regulated through the thermal stimuli.[125] In the NO_3RR involving multi-PCET, electron transfer can be modulated through electrochemical methods. However, the proton transfer steps in the hydrogenation process cannot be controlled by the electric potential. Therefore, the introduction of thermal stimuli presents a promising approach for synergistically regulating both electron and proton transfer processes.

Yu and colleagues[125] dispersed Ni on a Cu substrate to prevent the accumulation of localized active hydrogen, synthesizing Ni-decorated Cu single-atom alloy oxide nanowire (Ni_1Cu SAAO NW) to suppress the competing HER in NH_3 production from NO_3^-. While inhibiting side reactions by enhancing the active hydrogen coverage, merely applying voltage alone cannot promote proton transfer in the hydrogenation process effectively. Therefore, they introduced thermal stimuli to facilitate the conversion of NO_3^- (Fig. 10a), enhance water molecule dissociation, and reduce the energy barrier in the reaction. Compared with Cu_2O NWs under room temperature, Ni_1Cu SAAO NWs exhibited significantly enhanced activity and selectivity in alkaline electrolytes at 60–80 °C (Fig. 10b and c). As shown in Fig. 10d, even at 0.1 V *vs.* RHE, the faradaic efficiency of NH_3 production and temperature showed a positive correlation, increasing from 34.6% at 25 °C to 79.8% at 80 °C, with an NH_3 yield rate of 9.7 mg h^{-1} cm^{-2}. In contrast, with increasing temperature, Cu_2O NWs showed only limited improvement in faradaic efficiency. Furthermore, Fig. 10e illustrates the performance of NO_3^- to NO_2^- conversion at different temperatures. With increasing temperature, Ni_1Cu SAAO NWs demonstrated a gradual decrease in NO_2^- faradaic efficiency and yield rate, indicating that introducing thermal stimuli promoted the conversion of NO_3^- to NH_3. Conversely, Cu_2O exhibited a noticeable increase in NO_2^- yield with increasing temperature, maintaining a relatively high level of NO_2^- faradaic efficiency. This suggests that introducing thermal stimuli also promoted the reduction of NO_3^- to NO_2^- on Cu_2O NWs, but the relatively weak hydrogen affinity of Cu_2O NWs limited further performance enhancement.

Singh and colleagues[126] compared the thermal catalytic and electrocatalytic mechanisms of Pt/C, PtRu/C, and $Pt_{75}Ru_{25}$/C under different electrochemical reaction parameters, demonstrating the promoting effect of thermal stimuli in NH_3 production from NO_3RRs. They proposed that increasing the hydrogen (electro)chemical potential could enhance the conversion rate of NO_3^- (Fig. 10f). Furthermore, changes in pH significantly influenced the reaction performance of thermal catalysis and electrocatalysis in synthesizing NH_3 (Fig. 10g). The NH_3 yield rate of PtRu/C *via* thermal catalysis and electrocatalysis was also compared with industrial Haber–Bosch processes regarding rate and cost. As shown in Fig. 10h, the results indicated that the NH_3 yield rate of PtRu/C under pH = 1 was comparable to the Haber–Bosch process, with lower standard costs per ton of NH_4NO_3 consumed.

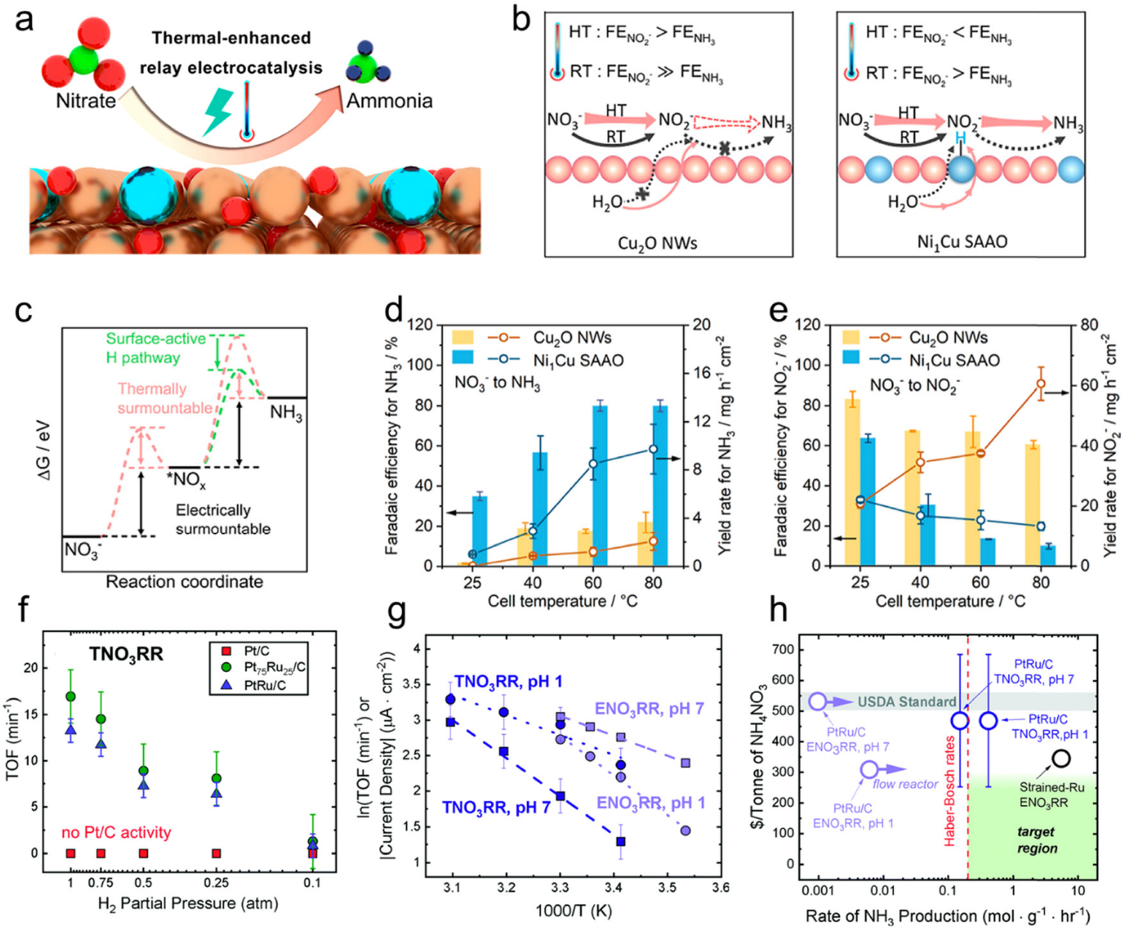

Fig. 10 (a) Thermal-assisted electrocatalysis NO_3RRs on Ni_1Cu SAAO NWs. (b) Mechanism diagram of the NO_3RR at different temperatures using Ni_1Cu SAAO and Cu_2O NWs. HT, RT, and FE are high temperature, room temperature, and faradaic efficiency, respectively. (c) The energy barrier overcome by thermally boosted electrocatalysis and surface-active hydrogen during NO_3^- reduction on Ni_1Cu SAAO. Faradaic efficiency and yield rate for (d) NH_3 and (e) NO_2^- production at different temperatures using Ni_1Cu SAAO and Cu_2O NWs at 0.1 V *vs.* RHE. Reproduced with permission.[125] Copyright 2024, American Chemical Society. (f) The activity of various catalysts in thermocatalytic NO_3RR at different H_2 partial pressures in pH 7 solution with 0.1 M $NaNO_3$. (g) Arrhenius plots of PtRu/C for thermocatalytic and electrocatalytic NO_3RRs. (h) The cost per tonne of NH_4NO_3 in thermocatalytic and electrocatalytic NO_3RRs *vs.* NH_3 yield rate. Reproduced with permission.[126] Copyright 2021, Royal Society of Chemistry.

5. Conclusion and outlook

In this review, we comprehensively summarized strategies involving a built-in electric field and external stimuli to enhance the performance of the NO_3RR for NH_3 production. The approach of introducing built-in electric fields includes the construction of Mott–Schottky heterojunctions, semiconductor–semiconductor heterojunctions, modulation of coordination structures for active sites, and the construction of double layers. Additionally, the external stimuli modulation strategies such as introducing optical, stress, and thermal stimuli for enhancing NH_3 production *via* NO_3RR were also summarized. Thoughtful design of built-in electric fields and external stimuli can effectively boost both the activity and selectivity of NH_3 production, with the potential to address energy crises and environmental pollution simultaneously. However, due to limited characterization techniques and design strategies, such modulation in the NO_3RR still faces significant challenges.

(1) Designing advanced characterization techniques to elucidate the specific roles of built-in electric field and external stimuli is crucial. For instance, introducing optical stimuli triggers the LSPR effect, generating high-energy hot electrons and holes and strong electric fields. However, distinguishing and quantifying the contributions of high-energy hot electrons and electric fields to catalytic reactions is challenging. Similarly, in semiconductor photocatalysis, light illumination induces the generation of carriers, accompanied by localized temperature changes on the electrode surface. Understanding the varying degrees of contribution from different enhancement mechanisms to catalysis facilitates the design of more efficient strategies to enhance catalytic efficiency.

(2) Developing *in situ* testing techniques is crucial for reactions involving built-in electric fields and external stimuli. Catalytic processes primarily occur on the catalyst surface, where such modulation can influence the adsorption and activation of reactants and intermediates, as well as control product distribution. *In situ* testing with built-in electric field/external stimuli participation can deepen the understanding of how they regulate catalytic processes. Catalytic reactions can be monitored in real-time, allowing observation of intermediate species behavior and changes in reaction kinetics. In short, developing *in situ* testing techniques will be pivotal in propelling the NO_3RR, offering real-time insights into reaction mechanisms, catalyst performance, and reaction dynamics. This progress will aid in designing enhanced and environmentally friendly NH_3 synthesis procedures.

(3) Optimize the methods of introducing external stimuli. For instance, stress stimuli are introduced primarily through ultrasonic waves. Nonetheless, it is vital to adjust catalyst structures and investigate approaches that make materials more responsive to external influences, allowing the piezoelectric effect to be activated by natural stimulation like water flow or wind pressure. Utilizing these natural disturbances augments the applicability of piezoelectric catalysis for enhancing NH_3 production efficiency. Moreover, as a distinctive piezoelectric material, ferroelectric materials possess inherent polarization, creating an internal electric field that originates from the collective polarization effect formed by the spontaneous alignment of electric dipoles. Pre-treating ferroelectric materials and introducing electric fields to facilitate the NO_3RR for NH_3 synthesis could also be an effective approach.

(4) Designing cost-effective catalysts in NH_3 production. For instance, using noble metals as the electrode material increases the cost of the NO_3RR in LSPR-assisted NH_3 production. Therefore, developing non-noble metal alternatives and designing effective strategies to amplify their LSPR effects and utilize high-energy hot electrons and strong electric fields to enhance NH_3 synthesis is crucial for reducing the cost associated with this approach. One promising avenue is the exploration of plasmonic nanostructures composed of non-noble metals, such as Cu and Al. These materials also possess unique plasmonic properties that can be harnessed to enhance the NO_3RR. By precisely tailoring the size, shape, and composition of these nanostructures, it is possible to tune their LSPR to the desired wavelength range for efficient NH_3 synthesis. Additionally, synergistic coupling of LSPR with other catalytic mechanisms can further enhance the efficiency of NH_3 synthesis. Integrating non-noble metal plasmonic nanostructures with suitable cocatalysts or semiconductors makes it feasible to harness the high-energy hot electrons generated during LSPR excitation and leverage the strong electric fields for selective and efficient NH_3 production. Developing cost-effective strategies for LSPR-assisted NH_3 synthesis using non-noble metals is essential for realizing sustainable and economically viable NH_3 production processes. Continued research in this direction has great promise for reducing the overall cost and improving the scalability of LSPR-based NH_3 synthesis technologies.

(5) In the research on regulating the NO_3RR to produce NH_3 through built-in electric field/external stimuli, exploring the coupling of multiple field/stimuli to enhance NH_3 production performance has significant importance and promising prospects. A variety of built-in electric fields, produced by Motte–Schottky heterojunctions, semiconductor–semiconductor heterojunctions, coordinated active site environments, and electrical double-layer modulation, along with external stimuli, including optical, stress, and thermal stimuli, can synergistically enhance one another when introduced simultaneously. This synergy influences the reaction kinetics and site activity, ultimately enhancing the efficiency of NH_3 production. Indeed, in the reaction of water splitting, studies have utilized the electric field generated by stress stimuli to further enhance the effective separation of photogenerated carriers, synergistically promoting reaction kinetics with the photogenerated electric field. In conclusion, by developing the combined effects of various field/stimuli, precise control over the catalytic process can be achieved, leading to improved performance in NH_3 production.

(6) Developing theoretical computations is pivotal for designing rational strategies to modulate catalytic reactions using built-in electric field/external stimuli. Current theoretical models still exhibit significant discrepancies between simulating fields and actual systems, posing substantial challenges in designing built-in electric field/external stimuli-assisted reaction strategies. Therefore, optimizing theoretical methods to more precisely predict the atomic configurations and band

structures of catalysts may obtain catalysts with higher performance. Meanwhile, tailored theoretical models can be explored for different fields to accurately assess the impact of built-in electric field/external stimuli on enhancing the performance of the NO_3RR for NH_3 synthesis from a theoretical perspective, elucidating their mechanisms. Machine learning can be employed to establish correlations between various built-in electric field/external stimuli and catalytic activity and selectivity, facilitating the identification of more suitable strategies.

(7) Developing stable catalysts. Stability is a crucial metric for evaluating catalyst performance. By designing catalysts with structural stability and employing methods to regulate the catalyst microenvironment for extending the catalyst's lifespan, there is potential to better adapt to external stimuli and to carry out NO_3RRs for NH_3 production under varying pH environments. Furthermore, common stability tests often consist of only a few dozen or even just a few cycles, which may not adequately reflect the catalyst's stability. Extending stability tests for longer durations until performance degradation occurs can help explore the catalyst's limit of stability, enabling rational design of the catalyst. Moreover, enhancing the stability of catalysts through strategic approaches can significantly increase their potential for industrial applications.

(8) A well-designed reactor effectively achieves high performance in reducing NO_3^- to produce NH_3. One potential direction for future research is introducing a flow cell system into the NO_3RR. The flow cells allow for continuous and controlled flow of reactants, enhancing mass transfer and improving reaction kinetics. This may lead to higher conversion rates and improved selectivity of electrochemical systems. Additionally, using flow cells enables better control of reaction conditions such as temperature, pressure, and flow rate, which is conducive to introducing external stimuli. Moreover, integrating flow cells can facilitate online monitoring and characterization techniques. This real-time monitoring capability can provide deeper insights into reaction kinetics, offering valuable insights for process optimization and catalyst design. Furthermore, flow cell systems can be easily scaled up for industrial applications, making it a promising approach for large-scale electrochemical NH_3 synthesis. In conclusion, the application of flow cells in the NO_3RR has the potential for improving reaction kinetics, better control of reaction conditions, enhanced online monitoring capabilities, and scalability for industrial implementation. Further research and development in this area will contribute to the advancement of efficient and practical NH_3 production technologies.

Data availability

No primary research results, software or code have been included and no new data were generated or analysed as part of this review.

Conflicts of interest

There are no conflicts of interest to declare.

References

1 Y. Xiong, Y. Wang, J. Zhou, F. Liu, F. Hao and Z. Fan, *Adv. Mater.*, 2024, **36**, 2304021.

2 S. Han, H. Li, T. Li, F. Chen, R. Yang, Y. Yu and B. Zhang, *Nat. Catal.*, 2023, **6**, 402–414.

3 S. Zhang, H. Hong, R. Zhang, Z. Wei, Y. Wang, D. Chen, C. Li, P. Li, H. Cui, Y. Hou, S. Wang, J. C. Ho, Y. Guo, Z. Huang and C. Zhi, *Angew. Chem.*, 2024, e202412830.

4 Z. Y. Wu, M. Karamad, X. Yong, Q. Huang, D. A. Cullen, P. Zhu, C. Xia, Q. Xiao, M. Shakouri, F. Y. Chen, J. Y. T. Kim, Y. Xia, K. Heck, Y. Hu, M. S. Wong, Q. Li, I. Gates, S. Siahrostami and H. Wang, *Nat. Commun.*, 2021, **12**, 2870.

5 Y. Guo, J. Gu, R. Zhang, S. Zhang, Z. Li, Y. Zhao, Z. Huang, J. Fan, Z. Chen and C. Zhi, *Adv. Energy Mater.*, 2021, **11**, 2101699.

6 H. Huang, K. Peramaiah and K.-W. Huang, *Energy Environ. Sci.*, 2024, **17**, 2682–2685.

7 L. Li, C. Tang, X. Cui, Y. Zheng, X. Wang, H. Xu, S. Zhang, T. Shao, K. Davey and S. Z. Qiao, *Angew. Chem.*, 2021, **133**, 14250–14256.

8 R. Zhang, H. Hong, X. Liu, S. Zhang, C. Li, H. Cui, Y. Wang, J. Liu, Y. Hou, P. Li, Z. Huang, Y. Guo and C. Zhi, *Angew. Chem., Int. Ed.*, 2023, **62**, e202309930.

9 Y. Kong, Y. Li, X. Sang, B. Yang, Z. Li, S. Zheng, Q. Zhang, S. Yao, X. Yang, L. Lei, S. Zhou, G. Wu and Y. Hou, *Adv. Mater.*, 2022, **34**, 2103548.

10 D. F. Abbott, Y. Z. Xu, D. A. Kuznetsov, P. Kumar, C. R. Müller, A. Fedorov and V. Mougel, *Angew. Chem.*, 2023, **135**, e202313746.

11 R. Zhang, Y. Guo, S. Zhang, D. Chen, Y. Zhao, Z. Huang, L. Ma, P. Li, Q. Yang, G. Liang and C. Zhi, *Adv. Energy Mater.*, 2022, **12**, 2103872.

12 Q. Hu, Y. Qin, X. Wang, Z. Wang, X. Huang, H. Zheng, K. Gao, H. Yang, P. Zhang, M. Shao and C. He, *Energy Environ. Sci.*, 2021, **14**, 4989–4997.

13 Y. Guo, R. Zhang, S. Zhang, Y. Zhao, Q. Yang, Z. Huang, B. Dong and C. Zhi, *Energy Environ. Sci.*, 2021, **14**, 3938–3944.

14 H. Zhang, C. Wang, H. Luo, J. Chen, M. Kuang and J. Yang, *Angew. Chem., Int. Ed.*, 2023, **62**, e202217071.

15 F.-Y. Chen, Z.-Y. Wu, S. Gupta, D. J. Rivera, S. V. Lambeets, S. Pecaut, J. Y. T. Kim, P. Zhu, Y. Z. Finfrock, D. M. Meira, G. King, G. Gao, W. Xu, D. A. Cullen, H. Zhou, Y. Han, D. E. Perea, C. L. Muhich and H. Wang, *Nat. Nanotechnol.*, 2022, **17**, 759–767.

16 M. Cui, L. Zeng, W. Qin and J. Feng, *Environ. Pollut.*, 2020, **263**, 114553.

17 B. Chen, E. Liu, Q. Tian, C. Yan and Y. Zhang, *Agron. Sustainable Dev.*, 2014, **34**, 429–442.

18 M. J. Hendry, L. I. Wassenaar, S. L. Barbour, M. S. Schabert, T. K. Birkham, T. Fedec and E. E. Schmeling, *Sci. Total Environ.*, 2018, **640**, 127–137.

19 D. Chen, S. Zhang, D. Yin, Q. Quan, Y. Zhang, W. Wang, Y. Meng, X. Liu, S. Yip, T. Yanagida, C. Zhi and J. C. Ho, *Chem Catal.*, 2024, **4**, 101024.

20 L. Bai, F. Franco, J. Timoshenko, C. Rettenmaier, F. Scholten, H. S. Jeon, A. Yoon, M. Rüscher, A. Herzog, F. T. Haase, S. Kühl, S. W. Chee, A. Bergmann and R. C. Beatriz, *J. Am. Chem. Soc.*, 2024, **146**, 9665–9678.

21 X. Zhao, M. Liu, Y. Wang, Y. Xiong, P. Yang, J. Qin, X. Xiong and Y. Lei, *ACS Nano*, 2022, **16**, 19959–19979.

22 K. Kim, A. Zagalskaya, J. L. Ng, J. Hong, V. Alexandrov, T. A. Pham and X. Su, *Nat. Commun.*, 2023, **14**, 823.

23 R. Zhang, Y. Zhang, B. Xiao, S. Zhang, Y. Wang, H. Cui, C. Li, Y. Hou, Y. Guo, T. Yang, J. Fan and C. Zhi, *Angew. Chem., Int. Ed.*, 2024, **63**, e202407589.

24 K. Fan, W. Xie, J. Li, Y. Sun, P. Xu, Y. Tang, Z. Li and M. Shao, *Nat. Commun.*, 2022, **13**, 7958.

25 D. Chen, S. Zhang, X. Bu, R. Zhang, Q. Quan, Z. Lai, W. Wang, Y. Meng, D. Yin, S. Yip, C. Liu, C. Zhi and J. C. Ho, *Nano Energy*, 2022, **98**, 107338.

26 J. Lim, C.-Y. Liu, J. Park, Y.-H. Liu, T. P. Senftle, S. W. Lee and M. C. Hatzell, *ACS Catal.*, 2021, **11**, 7568–7577.

27 G. Zhang, X. Li, K. Chen, Y. Guo, D. Ma and K. Chu, *Angew. Chem., Int. Ed.*, 2023, **62**, e202300054.

28 Y.-Y. Lou, Q.-Z. Zheng, S.-Y. Zhou, J.-Y. Fang, O. Akdim, X.-Y. Ding, R. Oh, G.-S. Park, X. Huang and S.-G. Sun, *ACS Catal.*, 2024, **14**, 5098–5108.

29 H. Du, H. Guo, K. Wang, X. Du, B. A. Beshiwork, S. Sun, Y. Luo, Q. Liu, T. Li and X. Sun, *Angew. Chem.*, 2023, **135**, e202215782.

30 R. Daiyan, T. Tran-Phu, P. Kumar, K. Iputera, Z. Tong, J. Leverett, M. H. A. Khan, A. A. Esmailpour, A. Jalili, M. Lim, A. Tricoli, R.-S. Liu, X. Lu, E. Lovell and R. Amal, *Energy Environ. Sci.*, 2021, **14**, 3588–3598.

31 H. Liu, X. Lang, C. Zhu, J. Timoshenko, M. Rüscher, L. Bai, N. Guijarro, H. Yin, Y. Peng, J. Li, Z. Liu, W. Wang, B. R. Cuenya and J. Luo, *Angew. Chem., Int. Ed.*, 2022, **61**, e202202556.

32 D. Chen, S. Zhang, D. Yin, W. Li, X. Bu, Q. Quan, Z. Lai, W. Wang, Y. Meng, C. Liu, S. Yip, F.-R. Chen, C. Zhi and J. C. Ho, *Adv. Energy Mater.*, 2023, **13**, 2203201.

33 L. Sun and B. Liu, *Adv. Mater.*, 2023, **35**, 2207305.

34 A. Paliwal, C. D. Bandas, E. S. Thornburg, R. T. Haasch and A. A. Gewirth, *ACS Catal.*, 2023, **13**, 6754–6762.

35 W. J. Sun, H. Q. Ji, L. X. Li, H. Y. Zhang, Z. K. Wang, J. H. He and J. M. Lu, *Angew. Chem., Int. Ed.*, 2021, **60**, 22933–22939.

36 X. Zhu, C. Ma, Y.-C. Wang, K. Qu, L. Song, J. Wang, Y. Gong, X. Liu, J. Zhang, Q. Lu and A.-L. Wang, *Energy Environ. Sci.*, 2024, **17**, 2908–2920.

37 X. Lv, T. Mou, J. Li, L. Kou and T. Frauenheim, *Adv. Funct. Mater.*, 2022, **32**, 2201262.

38 W. Wen, S. Fang, Y. Zhou, Y. Zhao, P. Li and X. Y. Yu, *Angew. Chem., Int. Ed.*, 2024, **63**, e202408382.

39 E. Contreras, R. Nixon, C. Litts, W. Zhang, F. M. Alcorn and P. K. Jain, *J. Am. Chem. Soc.*, 2022, **144**, 10743–10751.

40 R. Zhang, C. Li, H. Cui, Y. Wang, S. Zhang, P. Li, Y. Hou, Y. Guo, G. Liang, Z. Huang, C. Peng and C. Zhi, *Nat. Commun.*, 2023, **14**, 8036.

41 M. T. de Groot and M. T. M. Koper, *J. Electroanal. Chem.*, 2004, **562**, 81–94.

42 X. Zhang, Y. Wang, C. Liu, Y. Yu, S. Lu and B. Zhang, *Chem. Eng. J.*, 2021, **403**, 126269.

43 S. Garcia-Segura, M. Lanzarini-Lopes, K. Hristovski and P. Westerhoff, *Appl. Catal., B*, 2018, **236**, 546–568.

44 H. Luo, S. Li, Z. Wu, Y. Liu, W. Luo, W. Li, D. Zhang, J. Chen and J. Yang, *Adv. Mater.*, 2023, **35**, 2304695.

45 J. Zhou, M. Wen, R. Huang, Q. Wu, Y. Luo, Y. Tian, G. Wei and Y. Fu, *Energy Environ. Sci.*, 2023, **16**, 2611–2620.

46 G. E. Dima, A. C. A. de Vooys and M. T. M. Koper, *J. Electroanal. Chem.*, 2003, **554**, 15–23.

47 J. Long, S. Chen, Y. Zhang, C. Guo, X. Fu, D. Deng and J. Xiao, *Angew. Chem., Int. Ed.*, 2020, **59**, 9711–9718.

48 A. C. A. de Vooys, M. T. M. Koper, R. A. Van Santen and J. A. R. Van Veen, *J. Catal.*, 2001, **202**, 387–394.

49 A. C. A. de Vooys, G. L. Beltramo, B. Van Riet, J. A. R. Van Veen and M. T. M. Koper, *Electrochim. Acta*, 2004, **49**, 1307–1314.

50 J. Yang, M. Duca, K. J. P. Schouten and M. T. M. Koper, *J. Electroanal. Chem.*, 2011, **662**, 87–92.

51 R. Zhang, D. Shuai, K. A. Guy, J. R. Shapley, T. J. Strathmann and C. J. Werth, *ChemCatChem*, 2013, **5**, 313–321.

52 S. Liang, X. Teng, H. Xu, L. Chen and J. Shi, *Angew. Chem.*, 2024, **136**, e202400206.

53 O. Peng, Q. Hu, X. Zhou, R. Zhang, Y. Du, M. Li, L. Ma, S. Xi, W. Fu, Z.-X. Xu, C. Cheng, Z. Chen and K. P. Loh, *ACS Catal.*, 2022, **12**, 15045–15055.

54 A. C. A. de Vooys, M. T. M. Koper, R. A. Van Santen and J. A. R. Van Veen, *J. Electroanal. Chem.*, 2001, **506**, 127–137.

55 T. Hu, C. Wang, M. Wang, C. M. Li and C. Guo, *ACS Catal.*, 2021, **11**, 14417–14427.

56 H. Shin, S. Jung, S. Bae, W. Lee and H. Kim, *Environ. Sci. Technol.*, 2014, **48**, 12768–12774.

57 J. Gao, B. Jiang, C. Ni, Y. Qi and X. Bi, *Chem. Eng. J.*, 2020, **382**, 123034.

58 R. Liu, H. Zhao, X. Zhao, Z. He, Y. Lai, W. Shan, D. Bekana, G. Li and J. Liu, *Environ. Sci. Technol.*, 2018, **52**, 9992–10002.

59 J. M. McEnaney, S. J. Blair, A. C. Nielander, J. A. Schwalbe, D. M. Koshy, M. Cargnello and T. F. Jaramillo, *ACS Sustainable Chem. Eng.*, 2020, **8**, 2672–2681.

60 Y. Xiong, M. Sun, S. Wang, Y. Wang, J. Zhou, F. Hao, F. Liu, Y. Yan, X. Meng, L. Guo, Y. Liu, S. Chu, Q. Zhang, B. Huang and Z. Fan, *Adv. Funct. Mater.*, 2024, 2420153.

61 Y. Xiong, Y. Wang, M. Sun, J. Chen, J. Zhou, F. Hao, F. Liu, P. Lu, X. Meng, L. Guo, Y. Liu, S. Xi, Q. Zhang, B. Huang and Z. Fan, *Adv. Mater.*, 2024, **36**, 2407889.

62 X. Deng, Y. Yang, L. Wang, X. Z. Fu and J. L. Luo, *Adv. Sci.*, 2021, **8**, 2004523.

63 Z. Fang, Z. Jin, S. Tang, P. Li, P. Wu and G. Yu, *ACS Nano*, 2022, **16**, 1072–1081.

64 P. Mondol, D. Panthi, A. J. A. Ayala, S. O. Odoh and C. J. Barile, *J. Mater. Chem. A*, 2022, **10**, 22428–22436.

65 D. M. Weekes, D. A. Salvatore, A. Reyes, A. Huang and C. P. Berlinguette, *Acc. Chem. Res.*, 2018, **51**, 910–918.

66 W. Luc, X. Fu, J. Shi, J.-J. Lv, M. Jouny, B. H. Ko, Y. Xu, Q. Tu, X. Hu, J. Wu, Q. Yue, Y. Liu, F. Jiao and Y. Kang, *Nat. Catal.*, 2019, **2**, 423–430.

67 X. Fu, *Chin. J. Catal.*, 2023, **53**, 8–12.
68 Y. Zou, Y. Yan, Q. Xue, C. Zhang, T. Bao, X. Zhang, L. Yuan, S. Qiao, L. Song, J. Zou, C. Yu and C. Liu, *Angew. Chem., Int. Ed.*, 2024, **63**, e202409799.
69 Y. Chen, X. Xia, L. Tian, M. Yin, L.-L. Zheng, Q. Fu, D. Wu and J.-P. Zou, *Chin. Chem. Lett.*, 2024, **35**, 109789.
70 M. Zhang, Z. Zhang, S. Zhang, Z. Zhuang, K. Song, K. Paramaiah, M. Yi, H. Huang and D. Wang, *ACS Catal.*, 2024, **14**, 10437–10446.
71 L. Min, S. Liping, H. Lihua and Z. Hui, *Appl. Catal., A*, 2024, **676**, 119650.
72 X. Ji, C. Ma, F. Zhang, X. He, X. Fan, J. Li, Z. Li, L. Ouyang, L. Zhang, T. Li, D. Zhao, Y. Wang, J. Zhang, Z. Cai, S. Sun, A. A. Alshehri, Q. Lu and X. Sun, *ACS Sustainable Chem. Eng.*, 2023, **11**, 2686–2691.
73 D. Xu, S.-N. Zhang, J.-S. Chen and X.-H. Li, *Chem. Rev.*, 2022, **123**, 1–30.
74 Z. Zhang and J. T. Yates Jr., *Chem. Rev.*, 2012, **112**, 5520–5551.
75 H. Zhang, R. Li, M. Humayun, Z. Huang, Y. Fu, Y. Cao, J. Duan, Y. A. Attia and C. Wang, *Mater. Chem. Front.*, 2024, **8**, 2811–2835.
76 P. Gao, Z. H. Xue, S. N. Zhang, D. Xu, G. Y. Zhai, Q. Y. Li, J. S. Chen and X. H. Li, *Angew. Chem., Int. Ed.*, 2021, **60**, 20711–20716.
77 X. Fan, D. Zhao, Z. Deng, L. Zhang, J. Li, Z. Li, S. Sun, Y. Luo, D. Zheng, Y. Wang, B. Ying, J. Zhang, A. A. Alshehri, Y. Lin, C. Tang, X. Sun and Y. Zheng, *Small*, 2023, **19**, 2208036.
78 Y. Zhou, W. Zhang, P. Guo, Y. Guo, J. Zhan, Y. Wang, B. Zhang, S. Zhang, L.-H. Zhang and F. Yu, *Inorg. Chem. Front.*, 2024, **11**, 3503–3510.
79 A. Balapure, J. R. Dutta and R. Ganesan, *RSC Appl. Interfaces*, 2024, **1**, 43–69.
80 Y. Xu, Y. Sheng, M. Wang, T. Ren, K. Shi, Z. Wang, X. Li, L. Wang and H. Wang, *J. Mater. Chem. A*, 2022, **10**, 16883–16890.
81 F. Zhou and G. Tao, *J. Phys. Chem. C*, 2023, **127**, 23180–23188.
82 T. Kou, M. Chen, F. Wu, T. J. Smart, S. Wang, Y. Wu, Y. Zhang, S. Li, S. Lall, Z. Zhang, Y.-S. Liu, J. Guo, G. Wang, Y. Ping and Y. Li, *Nat. Commun.*, 2020, **11**, 590.
83 S. Ajmal, A. Kumar, M. A. Mushtaq, M. Tabish, Y. Zhao, W. Zhang, A. S. Khan, A. Saad, G. Yasin and W. Zhao, *Small*, 2024, **20**, 2310082.
84 B. Pan, Y. Wang and Y. Li, *Chem Catal.*, 2022, **2**, 1267–1276.
85 S. Zhang, Z. Liu, D. Chen, Z. Guo and M. Ruan, *Chem. Eng. J.*, 2020, **395**, 125101.
86 Y. Fan, W. Ma, D. Han, S. Gan, X. Dong and L. Niu, *Adv. Mater.*, 2015, **27**, 3767–3773.
87 Y. Guo, J. Sun, T. Guo, Y. Liu and Z. Yao, *Angew. Chem., Int. Ed.*, 2024, **63**, e202319664.
88 C. Zhang, Z. C. Shao, X. L. Zhang, G. Q. Liu, Y. Z. Zhang, L. Wu, C. Y. Liu, Y. Pan, F. H. Su, M. R. Gao, Y. Li and S. H. Yu, *Angew. Chem., Int. Ed.*, 2023, **62**, e202305571.
89 J. Xue, M. Fujitsuka, T. Tachikawa, J. Bao and T. Majima, *J. Am. Chem. Soc.*, 2024, **146**, 8787–8799.
90 S. Zhang, D. Chen, P. Chen, R. Zhang, Y. Hou, Y. Guo, P. Li, X. Liang, T. Xing, J. Chen, Y. Zhao, Z. Huang, D. Lei and C. Zhi, *Adv. Mater.*, 2024, **36**, 2310776.
91 J. Yang, L. Li, C. Xiao and Y. Xie, *Angew. Chem., Int. Ed.*, 2023, **62**, e202311911.
92 X. Sun, S. Jiang, H. Huang, H. Li, B. Jia and T. Ma, *Angew. Chem., Int. Ed.*, 2022, **61**, e202204880.
93 Y. Chen, C. Yan, J. Dong, W. Zhou, F. Rosei, Y. Feng and L. N. Wang, *Adv. Funct. Mater.*, 2021, **31**, 2104099.
94 K. Wenderich and G. Mul, *Chem. Rev.*, 2016, **116**, 14587–14619.
95 H. Li, Y. Zhou, W. Tu, J. Ye and Z. Zou, *Adv. Funct. Mater.*, 2015, **25**, 998–1013.
96 E. Sharma, V. Thakur, S. Sangar and K. Singh, *Mater. Today: Proc.*, 2020, **32**, 584–593.
97 J. Li, R. Chen, J. Wang, Y. Zhou, G. Yang and F. Dong, *Nat. Commun.*, 2022, **13**, 1098.
98 D. Hao, J. Ren, Y. Wang, H. Arandiyan, M. Garbrecht, X. Bai, H. K. Shon, W. Wei and B.-J. Ni, *Energy Mater. Adv.*, 2021, **2021**, 9761263.
99 J. Homola, S. S. Yee and G. Gauglitz, *Sens. Actuators, B*, 1999, **54**, 3–15.
100 E. K. Payne, K. L. Shuford, S. Park, G. C. Schatz and C. A. Mirkin, *J. Phys. Chem. B*, 2006, **110**, 2150–2154.
101 C. L. Wong and M. Olivo, *Plasmonics*, 2014, **9**, 809–824.
102 E. Hutter and J. H. Fendler, *Adv. Mater.*, 2004, **16**, 1685–1706.
103 H. Ahn, H. Song, J.-R. Choi and K. Kim, *Sensors*, 2018, **18**, 98.
104 A. Agrawal, S. H. Cho, O. Zandi, S. Ghosh, R. W. Johns and D. J. Milliron, *Chem. Rev.*, 2018, **118**, 3121–3207.
105 K. A. Willets and R. P. Van Duyne, *Annu. Rev. Phys. Chem.*, 2007, **58**, 267–297.
106 T. Uwada, T. Asahi, H. Masuhara, D. Ibano, M. Fujishiro and T. Tominaga, *Chem. Lett.*, 2007, **36**, 318–319.
107 M. Ahlawat, D. Mittal and V. Govind Rao, *Commun. Mater.*, 2021, **2**, 114.
108 X. Yu, S. Du, Z. Xu, J. He, F. Liu, B. Wang, S. Sun, Y. Tang and K. Zhao, *Chem. Eng. J.*, 2024, **480**, 148152.
109 C. Song, Z. Wang, Z. Yin, D. Xiao and D. Ma, *Chem Catal.*, 2022, **2**, 52–83.
110 Z. Zheng, W. Xie, M. Li, Y. H. Ng, D.-W. Wang, Y. Dai, B. Huang and R. Amal, *Nano Energy*, 2017, **41**, 233–242.
111 S. S. Rayalu, D. Jose, M. V. Joshi, P. A. Mangrulkar, K. Shrestha and K. Klabunde, *Appl. Catal., B*, 2013, **142**, 684–693.
112 X. Xie, J. Feng, X. Cui, J. Liu, L. Jiang and L. Dong, *ACS Catal.*, 2021, **11**, 13160–13168.
113 Y. Ma, X. Han, S. Xu, Z. Wang, W. Li, I. Da Silva, S. Chansai, D. Lee, Y. Zou, M. Nikiel, P. Manuel, A. M. Sheveleva, F. Tuna, E. J. L. McInnes, Y. Cheng, S. Rudić, A. J. Ramirez-Cuesta, S. J. Haigh, C. Hardacre, M. Schröder and S. Yang, *J. Am. Chem. Soc.*, 2021, **143**, 10977–10985.
114 S. L. Wu and S. Yoo, *Nat. Rev. Phys.*, 2022, **4**, 143–144.
115 S. Li, Z. Zhao, J. Zhao, Z. Zhang, X. Li and J. Zhang, *ACS Appl. Nano Mater.*, 2020, **3**, 1063–1079.

116 R. Su, H. A. Hsain, M. Wu, D. Zhang, X. Hu, Z. Wang, X. Wang, F. T. Li, X. Chen, L. Zhu, Y. Yang, Y. Yang, X. Lou and S. J. Pennycook, *Angew. Chem., Int. Ed.*, 2019, **58**, 15076–15081.

117 Y. Zhu, H. Chen, L. Wang, L. Ye, H. Zhou, Q. Peng, H. Zhu and Y. Huang, *Chin. Chem. Lett.*, 2024, **35**, 108884.

118 J. Ma, S. Jing, Y. Wang, X. Liu, L. Y. Gan, C. Wang, J. Y. Dai, X. Han and X. Zhou, *Adv. Energy Mater.*, 2022, **12**, 2200253.

119 S. Zhang, D. Chen, Y. Guo, R. Zhang, Y. Zhao, Z. Huang, J. Fan, J. C. Ho and C. Zhi, *Mater. Today*, 2023, **66**, 17–25.

120 J. Zhang, K. Lv, J. Cheng, Y. Liu, Y. Wang, S.-F. Yin and P. Chen, *Appl. Catal., B*, 2025, **361**, 124558.

121 S. Yuan, Y. Li, J. Peng, Y. M. Questell-Santiago, K. Akkiraju, L. Giordano, D. J. Zheng, S. Bagi, Y. Román-Leshkov and Y. Shao-Horn, *Adv. Energy Mater.*, 2020, **10**, 2002154.

122 Y. Zhao, W. Gao, S. Li, G. R. Williams, A. H. Mahadi and D. Ma, *Joule*, 2019, **3**, 920–937.

123 J. Zhang, H. Chen, X. Duan, H. Sun and S. Wang, *Mater. Today*, 2023, **68**, 234–253.

124 S. Zhang, D. Chen, Z. Liu, M. Ruan and Z. Guo, *Appl. Catal., B*, 2021, **284**, 119686.

125 K. Liu, H. Li, M. Xie, P. Wang, Z. Jin, Y. Liu, M. Zhou, P. Li and G. Yu, *J. Am. Chem. Soc.*, 2024, **146**, 7779–7790.

126 Z. Wang, E. M. Ortiz, B. R. Goldsmith and N. Singh, *Catal. Sci. Technol.*, 2021, **11**, 7098–7109.